Vol. 18, No. 2, 2022

Journal of Global Positioning Systems

ISSN 1446-3156 (Print Version) ISSN 1446-3164 (CD-ROM Version)

International Association of Chinese Professionals in Global Positioning Systems (CPGPS)

Journal of Global Positioning Systems

Aims and Scope

The Journal of Global Positioning Systems is a peer-reviewed international journal for the publication of original research papers, review articles, invited contributions, also including selected papers presented at non-referred conferences and symposiums. Articles should present discussions of technologies and applications of any positioning systems, including Global Navigation Satellite Systems (GNSS) and their various augmentations and local components, and other positioning and navigation technologies, such as indoor positioning, and inertial, visual navigation systems and their integrations. Articles presenting advances of other related areas, such as wireless communications, intelligent vehicle systems, sensor networks, spatial information and geosciences are also welcome. Short research and technical notes, book reviews, lecture series and commercial advertisements can be included. Specific questions about the suitability of prospective manuscripts may be directed to the Editor-in-Chief.

Publication and Copyright

The Journal of Global Positioning Systems is an official publication of the International Association of Chinese Professionals in Global Positioning Systems (CPGPS). It is published twice a year, in June and December. The Journal is available in both print version (ISSN 1446-3156) and CD-ROM version (ISSN 1446-3164), which can be accessed through the CPGPS website at http://www.cpgps.org/journal.php. Whilst CPGPS owns all the copyright of all text material published in the Journal, the authors are responsible for the views and statements expressed in their articles. Neither the authors, the editors nor CPGPS can accept any legal responsibility for the contents published in the journal.

ISSN 1446-3156 (Print Version)/ISSN 1446-3164 (CD-ROM Version)

Journal of Global Positioning Systems
2022
© CPGPS

Journal of Global Positioning Systems

Published by
the International Association of Chinese Professionals
in Global Positioning Systems

Vol. 18, No. 2, 2022

Table of Contents

Articles

PhD Dissertation Abstracts

Journal of Global Positioning Systems (2022)
Vol. 18, No. 2: 92-102
DOI: 10.5081/jgps.18.2.92

Journal of Global Positioning Systems
2022

GNSS-IR Inshore Tide Measurement Based on Low-cost Chipset

Jie Li, Dongkai Yang, Feng Wang and Jin Xing
BeiHang university

Abstract: Multipath signals that impact positioning accuracy are progressively being utilized to recover land and ocean geophysical information with the introduction of Global Navigation Satellite Systems (GNSS). An interference signal-based approach is GNSS-interferometry reflectometry (GNSS-IR). In this work, interference signals are gathered for sea surface altimetry using a low-cost GNSS signal receiver outfitted with a right-handed circularly polarized antenna, which can reduce cost of tide measurement. This study decompose the raw signal-to-noise ratio and extracts several frequency components using an empirical mode decomposition technique. The vertical distance between the antenna phase center and the sea surface is then calculated using Lomb-Scargle periodogram after the spectra of various frequency components has been analyzed. The final inversion tide is then obtained by removing the wild spots using the sinusoidal fitting approach. According to the results, there is a 0.89 correlation between the measured and recovered tides, and the RMSE is 0.23 m.

Keywords: global navigation satellite systems interferometry reflectometry, tide, empirical mode decomposition, sinusoidal fitting

1. Introduction

Reliable inshore tide measurements are crucial for tourism, dock operations, and fisheries production[1]. Tide measurement stations, which are costly to build, are one of the conventional techniques of monitoring the tide[2]. With the benefits of extensive coverage, excellent accuracy, and no identifiable signal source, GNSS-IR altimetry uses reflected signal path delay to calculate height[3]. GNSS-IR has been used in the retrieval of soil moisture[4], measurement of vegetation growth state[5],, measurement of snow depth[6], and measurement of lake level[7].

In 1993, Martin-Neira developed the Passive Reflectometry and Interferometry System (PARIS) idea and employed interference signals created by direct and reflected signals from the sea surface to estimate sea surface height[8]. Based on the PARIS idea, Martin-Neira et al. conducted a GPS-R sea surface height measuring experiment in Amsterdam in 1997, and the outcomes supported the viability of obtaining sea surface height from satellite navigation signals[9].

GNSS-IR has been widely used to measure tides. A technique based on wavelet analysis and least squares estimate was presented by Wang et al. to rectify the arc height variation inaccuracy of a single SNR[10]. They used a location in Hong Kong, China, to evaluate the method's capacity to take height fluctuation error into account and prevent mistake inheritance. A signal processing-based quality control approach is suggested to handle LSP graphs with several comparable peaks. This approach combines a number of criteria with outside limitations. According to experimental results, this approach can successfully lower gross error and improve measurement accuracy[11]. From 2008 to 2020, Peng et al. installed GNSS observation stations in three coastal regions with various land motions to assess the sea surface height. Results indicate that, when

Editor-In-Charge: Dr. Caijun Xu

compared to *in-situ* tidal, the precision of daily mean sea surface height measurements is less than 1.5 cm, and the trend in time is comparable with *in-situ* tidal within the uncertainty range[12]. At Thule, Greenland, which is frequently impacted by icebergs and sea ice throughout the year, an experiment was carried out. The estimated uncertainty is 18 cm, however the root means square deviation (RMSD) is 13 cm[13]. A coherent integration time optimization model was created[14] in order to more accurately forecast how the accuracy of GNSS-IR altimetry varies with coherent integration time and eventually improve altimetry accuracy.

Due to the complicated sea conditions, sea waves and undercurrents may create several frequency components of GNSS interference signals, decreasing measurement accuracy. In order to investigate and perhaps address the multi-frequency mixing problem, researchers use signal processing techniques. By reducing the function of signal-to-noise ratio (SNR) noise, increasing the measurement accuracy of multipath frequency extracted from SNR data by Lomb-Scargle periodogram (LSP), and other methods, Wang et al. found that discrete wavelet decomposition can improve the performance of tide measurement[15]. The researchers then made the suggestion that in order to solve the problem that the elevation angle of the satellite significantly affects the tidal inversion of the GNSS interferometric signal, one could use the EMD technique to decompose SNR in order to produce an effective SNR residual sequence. They utilized data from the American SC02 and Australian RSBY databases to confirm the results[16]. The results show that EMD boosts GNSS data use and expands the range of GNSS interference signals that are usable. Hu et al. proposed a novel GNSS-IR tidal estimating model combined with variational mode decomposition (VMD)[17] using measured data from Sweden's Onsala Space Observatory. The results show that the model improves stability and accuracy, with a correlation value that can be close to 0.97.

This work employed a low-cost GNSS receiver to gather interference signals in order to lower the cost and increase the coverage of shore tidal monitoring. Many diffuse processes, such as waves and the roughness of the ocean surface, produce reflected signals with various frequency ranges. The raw interference signal was divided in this study using the empirical mode decomposition (EMD) method to produce the reflected signal with various frequencies as well as the DC component (direct signal). The spectrum of the reflected signals at various frequencies is then calculated using the LSP spectrum estimate technique. This work uses the sinusoidal fitting approach to fit the recovered sea surface height and removes the points with a large modulus from the fitting function since tidal fluctuation tends to be a sine function. The rest of this essay is organized as follows: The GNSS-IR sea level measurement theoretical premise is introduced in the second section. The experimental verification is done in the third section. The results are shown in the fourth section. The conclusion of the study is elaborated in the final section.

2. Methodology

Signals reflected by the sea surface can also be picked up by GNSS devices in addition to direct signals. Sea levels can be determined due to the knowledge about the sea surface contained in these reflected impulses. The electromagnetic pulse can be viewed as a plane wave given the great distance between land-based GNSS receivers and spacecraft. The layout of GNSS-IR altimetry is shown in Figure 1, and the total of the red lines represents the route delay between the reflected and direct signal.

The path delay of the direct reflection signal can be determined using the geometric correlations in Figure 1 as follows:

$$\delta = \frac{\mathrm{h}}{\sin\theta} - \frac{\mathrm{h}}{\sin\theta}\cos 2\theta \tag{1}$$

where h represents the height of the GNSS antenna and θ represents the satellite elevation angle. After simplified, Equation (1) can be written as:

$$\delta = 2h\sin\theta \tag{2}$$

The oscillation frequency of the interference signal with the satellite elevation angle sine as the

horizontal axis is:

$$f = \frac{d(\delta/\lambda)}{d\sin\theta} = \frac{2h}{\lambda} \quad (3)$$

wherein λ represents the wavelength of electro-magnetic wave.

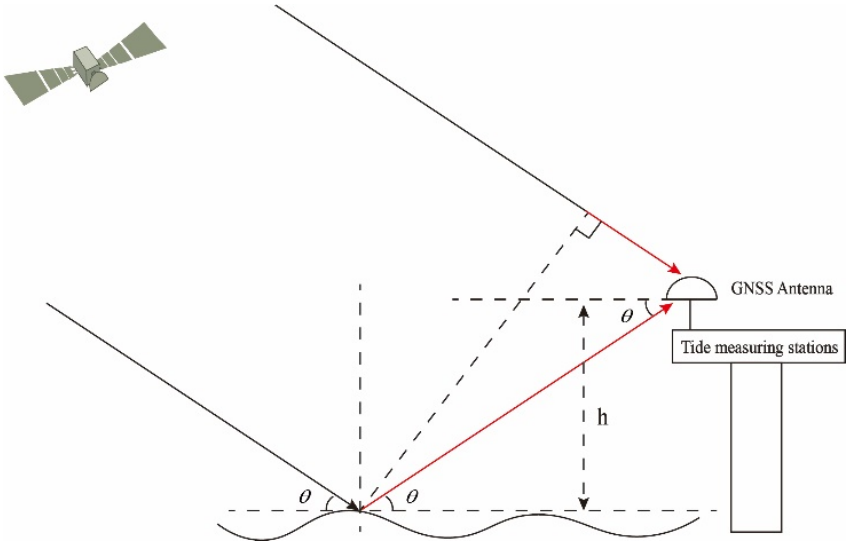

Figure 1 Geometry of GNSS-IR altimetry

Equation (3) states that the vertical separation between the antenna and the reflector determines the fluctuation frequency of the interference signal, which in turn relies on the height of the GNSS antenna. As a result, the sea level can be determined using the aforementioned hypothesis.

Due to the complicated nature of sea circumstances, reflected signals will have a range of various frequency components. The reflected signals from various reflectors should be successfully retrieved before height measurement. The signal is broken down into the total of several intrinsic mode functions using an approach known as empirical mode decomposition (EMD), which bases its time scale on the local features of the signal (IMF). EMD successfully extracts the feature information from the original signal while emphasizing the local characteristics of the reflected signals.

Signals that are reflected off the sea surface interact with direct signals; the interference signal's SNR is represented as:

$$SNR = A_d^2 + \sum_{i=1}^{n}(A_i^2 + A_d A_i \cos\varphi_i) \quad (4)$$

wherein A_d represents the amplitude of the direct signal, A_i represents the amplitude of *i-th* reflected signals, and φ_i represents the phase difference between direct and *i-th* reflected signals. According to the EMD theory, A_d is the residual component after the decomposition of n IMF components, the oscillating terms are different IMFs.

The processing of EMD is shown in Figure 2:

1) Initialization: $r(t) = x(t)$, $i = 0$, $k = 1$, the termination threshold condition is $\sigma = 0.2\sim0.3$, where $x(t)$ represents the raw SNR data, i means the number of iterations, and k means the serial number of IMF.

2) The local maximum and minimum points of $r(t)$ obtained; The upper and lower envelope $e_{\max}(t)$ and $e_{\min}(t)$ of the signal were obtained by fitting the maximum and minimum points respectively with cubic spline curves. The average envelope $m(t)$ was obtained by calculating the local mean values from the upper and lower envelope.

3) Let $i = i+1$, subtract the mean envelope from the raw signal to get the component to be identified:

$$p_i(t) = r(t) - m(t) \quad (5)$$

4) Calculate the termination iteration condition SD. It is generally impossible to completely realize the mean value of the upper and lower envelope to be 0. Normally, if $SD < \sigma$, let $IMF_k(t) = p_i(t)$ and go to the next step, or let $r(t) = p_i(t)$ and repeat the step (2)-(4).

5) Calculate $r(t) = r(t) - IMF_k(t)$, and Determine whether $r(t)$ is monotonic. If it is not, return to step (2) and execute $k = k + 1$ until $r(t)$ is a monotonic function. The final signal is decomposed into the following forms as Equation (4).

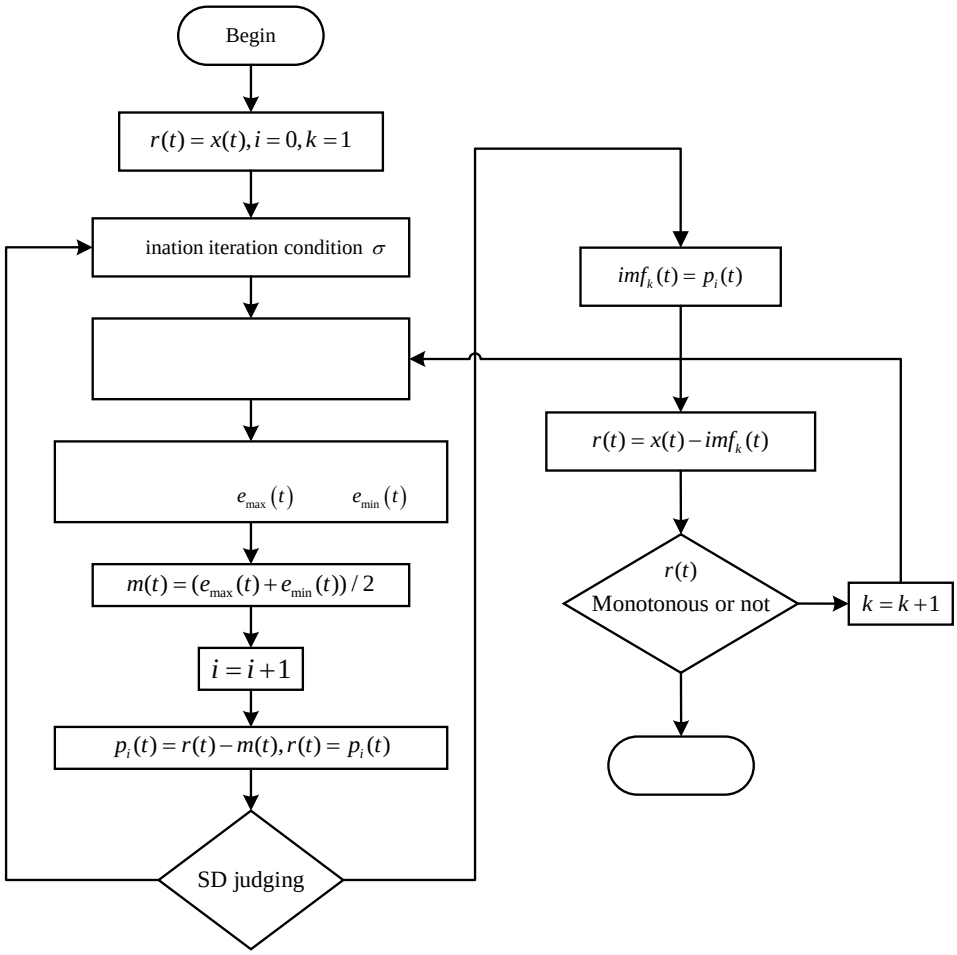

Figure 2 EMD flow diagram

Similar frequency components may still be present in the partial IMF following EMD decomposition, and the predicted and actual sea surface heights will vary significantly. This research used sinusoidal function fitting to acquire observed tidal trends and eliminate the wild areas because tides exhibit a sinusoidal trend. When there is a storm surge or a powerful sea surface breeze, the variation in sea level that GNSS-IR detects deviates from the sinusoidal rhythm. This part of the data can be marked as "unreliable" and excluded because GNSS-IR is presently unable to identify ocean height with any degree of reliability. Furthermore, if the data deviates from the sinusoidal pattern even for a short while, the sea surface might be having storm surge. This forecast method can be used as a new area of investigation in this study.

In this research, RHCP antenna is utilized. The primary polarization features of the reflected signal will change to LHCP when the satellite elevation angle is larger than the Brusset angle[1]. In this research, a scenario was run under the following circumstances: The tide height is and the distance between the GNSS station and sea level is 8 meters.

The modeling of interfering signal SNR is depicted in Figure 3. Low satellite height angles cause the SNR to clearly fluctuate. Additionally, the SNR fluctuates significantly due to the intricacy of the sea surface.

We decomposed the raw SNR using the EMD method, and the outcomes are depicted in Figure 4. The five panels on the right depict the corresponding LSP spectrum, while the five panels on the left show the IMF components (IMF1,4,5,6, and 7). The simulation results demonstrate that the EMD initially breaks down to produce high-frequency components before progressively decreasing in frequency. The sea surface reflects a large number of messages with high-frequency components. The height recorded by IMFs IMF5 and IMF6 should be the vertical distance between the GNSS antenna and sea surface, however, as the low-frequency component's highest value is around 8 m.

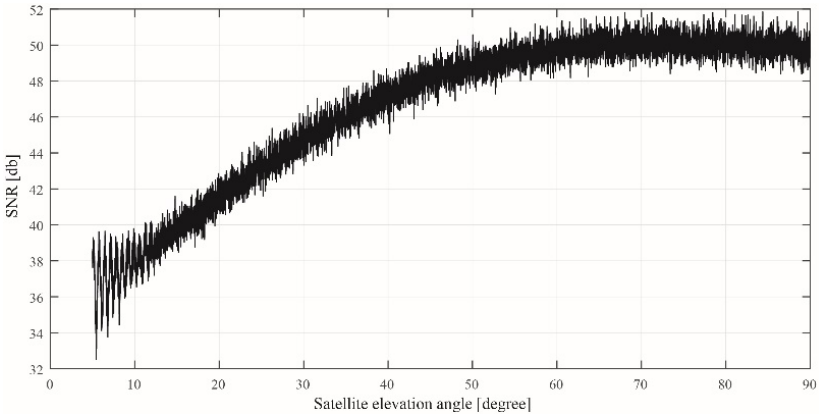

Figure 3 Simulation of interference signal SNR

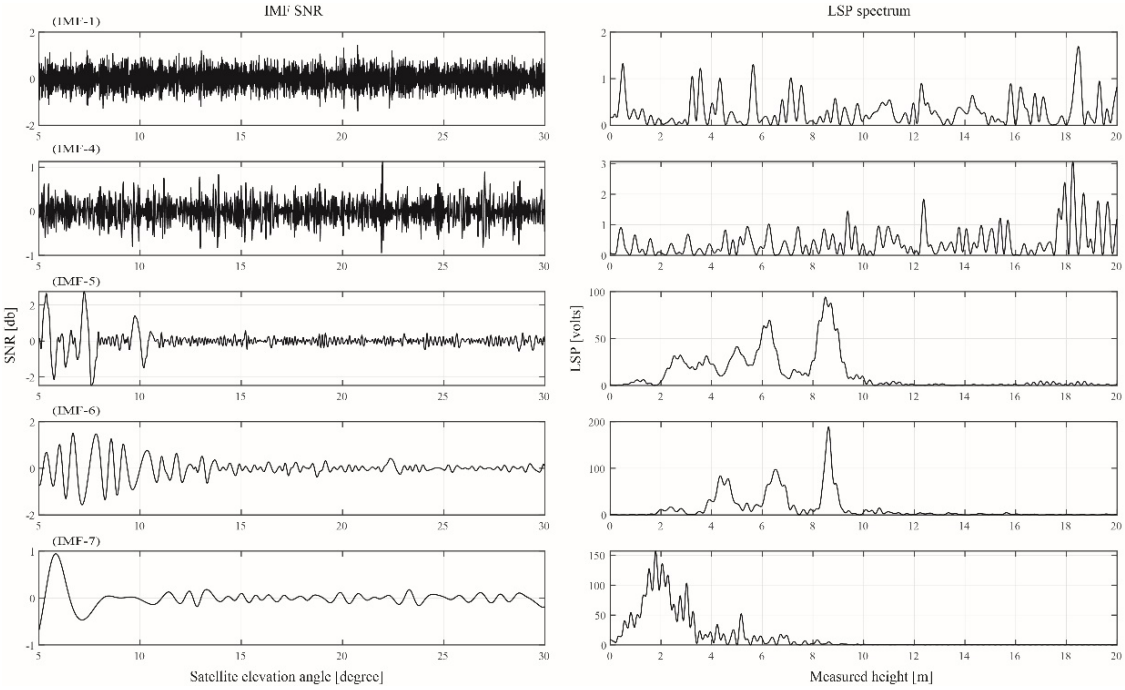

Figure 4 Simulation of IMF and LSP spectrum for raw interference signal SNR

The signal still contains frequency components after EMD that cannot be distinguished. In this investigation, anomalous inversion values were eliminated using sine fitting. Figure 4 displays two almost equal peaks for IMF-5 and IMF-6, which should be noted since they will affect the measurement. An IMF with a high peak power was employed for this experiment.

Figure 5 displays the results, with the measured height shown by the star mark, the fitting curve displayed by the black solid line, and the correct height indicated by the blue dashed line. It can be regarded as a wild point and eliminated when the modulus between the measured result and the fitted curve exceeds the threshold.

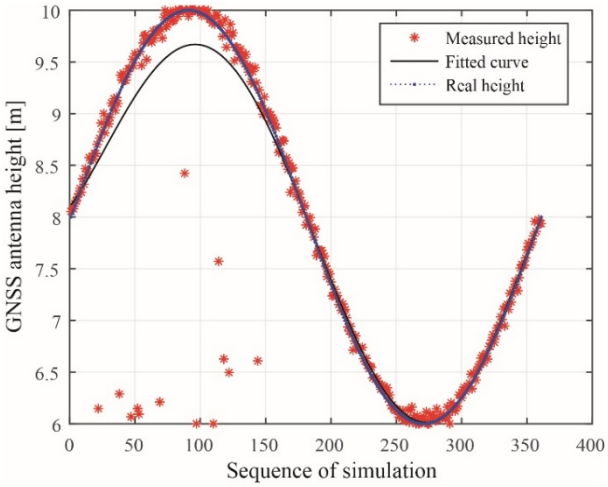

Figure 5 Simulation of measured and real height

3. Experiment

We conducted an experiment at Qingdong 5 tide measurement station in Dongying, Shandong Province. The location is 20 kilometers from eastern shoreline, the long-term sea breeze is mild, but there could be a brief storm surge. The coordinate of the station is ($37°26'51"N,119°0'36"E$), and the experiment period is November 2021. The GNSS antenna was installed towards the southwest, which is nearly 7m above the sea surface. The receiver was placed in a waterproof iron box, and the raw SNR of GNSS interference signal is recorded as a sample rate of 1s. The experiment site was shown in Figure 6, (a) is the experiment station, (b) is the ron box, (c) is the the GNSS antenna, and (d) is the low-cost GNSS chipset.

The satellite elevation angle is labeled on Figure 7 as the X-label, and the interference signal's raw SNR is labeled on the Y-axis. The SNR of the raw interference signal oscillates when the satellite's elevation angle is low. The oscillation vanishes when the satellite's elevation angle rises, which is consistent with the outcomes of the simulation. Therefore, in the data processing of this study, only the satellite elevation angle 5° to 25°, and azimuth 120° to 280° was selected.

Similarly, EMD are used to decompose various frequency components of interference signals' raw SNR. The results displayed in Figure 8 were obtained when LSP was used to determine the spectrum of IMF following decomposition. The results demonstrate that EMD is capable of decomposing signals into their constituent frequency components. Nonetheless, there are still frequency components that are aliased together in a complicated scenario like the ocean. Moreover, more distinction is required. In fact, we have excluded data with heights in the range of 5-10 m when dealing with retreived heights. To show more results, we have kept the LSP spectrum estimates for measured heights in the range of 0-20 m in Figure 8.

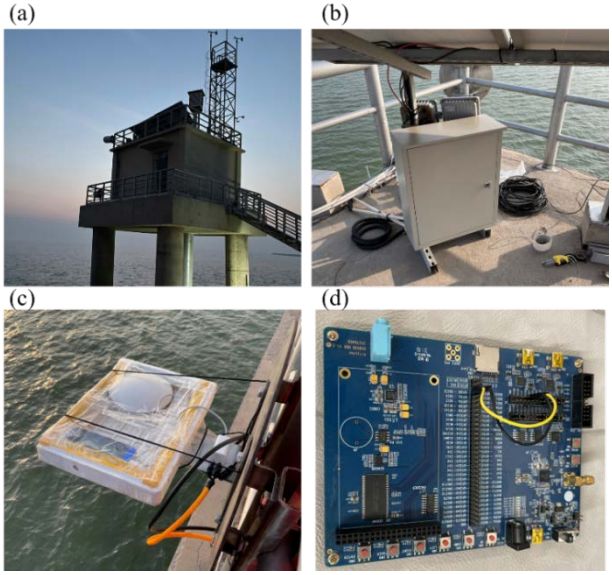

Figure 6 Experiment site

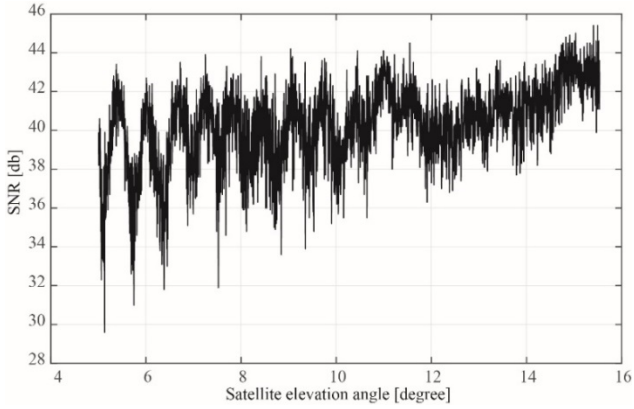

Figure 7 SNR of measured raw interference signal

Using the algorithm in this study, the trend comparison graph between the retrieved and the *in-situ* tide is obtained. As Figure 9 (a) shows that the retrieved and *in-situ* tide have a good agreement. The experimental station's wind speed record is displayed in Figure 9 (b). It is important to note that the measurements differ significantly around November 7. This is because the wind speed is stronger at this time (above 15m/s), which causes the signal character component to weaken and impact the measurement. Finally, the measurement error is shown in Figure 9 (c).

4. Results

To create the scatter plot seen in Figure 10, we use the retrieved tide as the Y-axis and the *in-situ* tide as the X-axis. The results reveal that the points are essentially distributed along the reference line $X=Y$, demonstrating a strong connection between the retrieved and observed tides. The measured and retrieved tides have a 0.89 correlation, and the RMSE is 0.23 m.

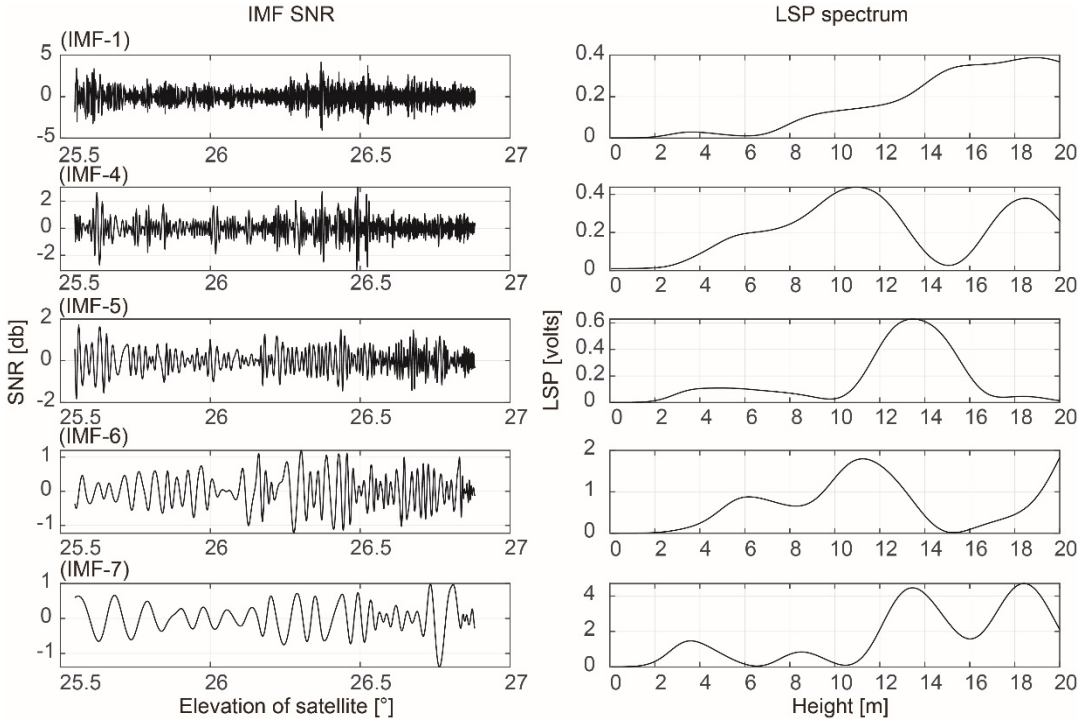

Figure 8 IMF and LSP spectrum for raw interference signal SNR

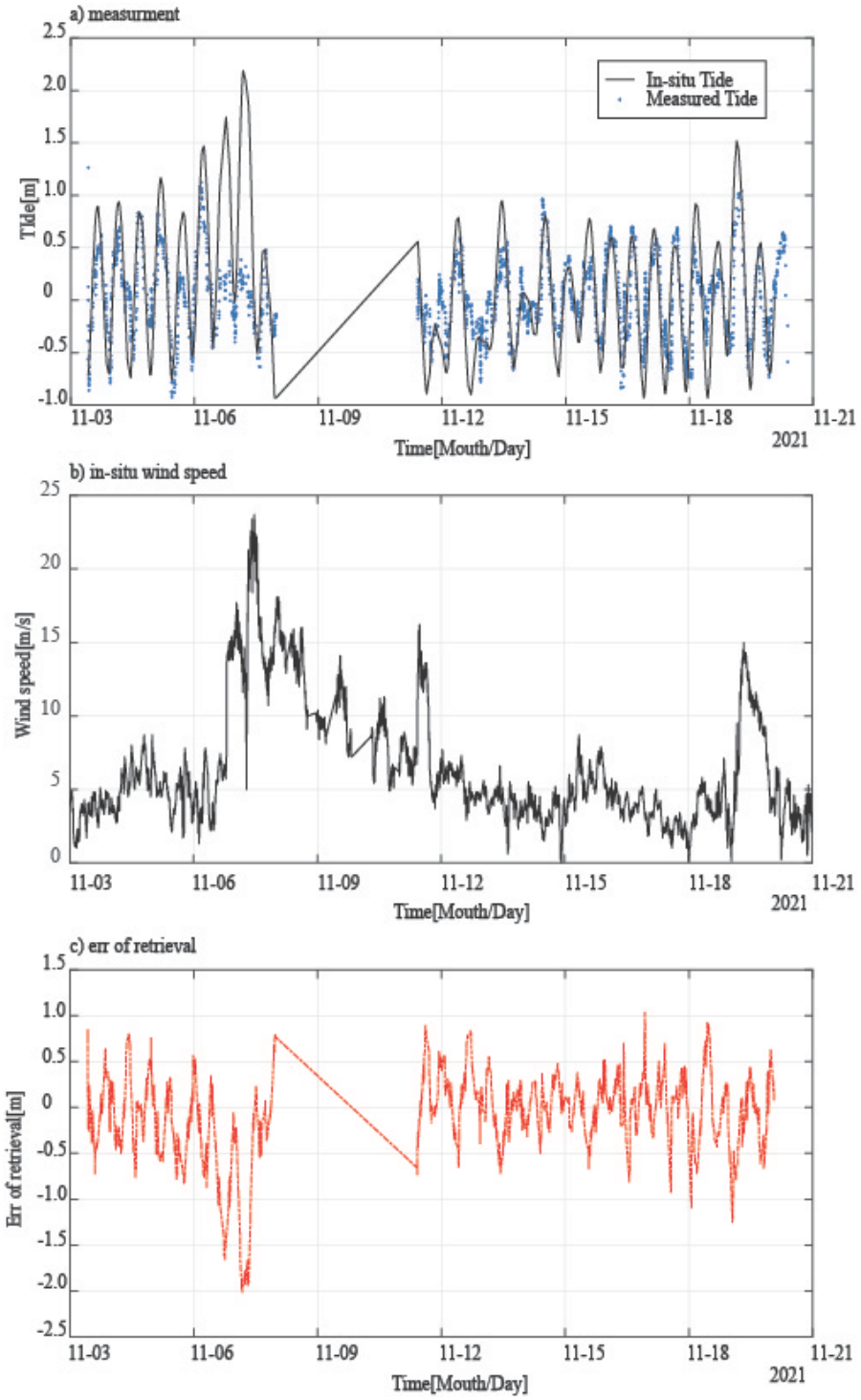

Figure 9 (a) Retrieved and *in-situ* tide change with time, (b) *in-situ* wind speed

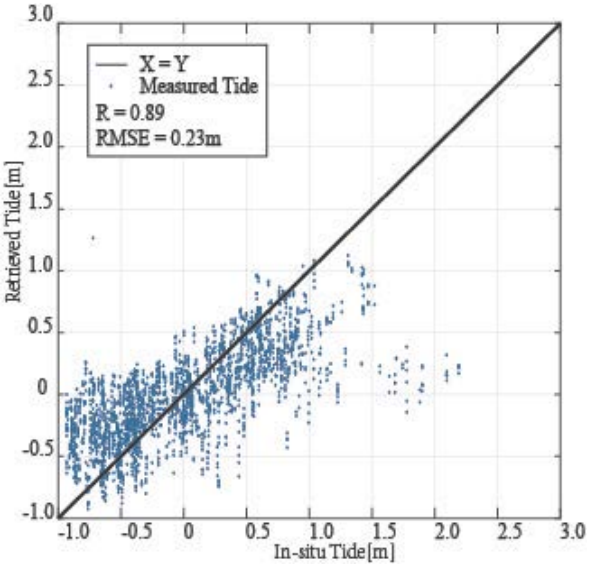

Figure 10 Scatter of retrieved and *in-situ* tide

5. Discussion

Since it was used for ground tracking, GNSS-IR has been extensively used in tide measurement. The benefits of GNSS-IR tide survey over conventional tide survey methods include easy installation and a large measuring window. This paper collects interference signals created by reflected on the sea surface and direct signals and records them in the form of SNR in order to further lower the monitoring cost. This paper's simulation and experiment confirm the viability of using low-cost GNSS receivers for measuring tides, which successfully enables widespread station dissemination.

More precise tide measurement can be obtained at a reduced expense by integrating GNSS-IR altimetry technology with conventional GNSS receivers. Additionally, the time needed to distribute tidal measuring stations based on GNSS-IR can be shortened while reducing the complexity of development. It is a significant area for growth in the realm of remote sensing.

6. Conclusion

There has been extensive usage of GNSS-IR retrieval of in-shore tide variations. In this study, a low-cost GNSS chipset is employed for tidal measurement in an effort to address issues with high cost, challenging large-scale receiver architecture, and the effect of storm surge on inversion accuracy. In this study, the raw SNR of GNSS interference signals was deposed into its various frequency components using EMD, and the estimated frequencies of the various signals were determined using LSP. In order to completely remove the impact of wild points and storm surge on measurement accuracy, the sinusoidal fitting approach was adopted.The single board utilized in this study costs less than 1000 RMB, and using only one antenna can further cut costs. Also, this inexpensive GNSS receiver and GNSS-IR technology combined can significantly lessen the issues with measurement precision brought on by crustal displacement, which is a common tendency of future growth.

7. Reference

[1]. Ghosh, Surajit & Hazra, Sugata & Nandy, Subrata & Mondal, Partho & Watham, Taibanganba & Kushwaha, Satya. (2017). Trends of sea level in the Bay of Bengal using altimetry and other complementary techniques. Journal of Spatial Science. 63. 1-14. 10.1080/14498596.2017.1348309.

[2]. Zheng, Naiquan & Chen, Peng & Li, Zheng. (2021). Accuracy analysis of ground-based GNSS-R sea level monitoring based on multi GNSS and multi SNR. Advances in Space Research. 68. 10.1016/j.asr.2021.04.024.

[3]. Martin-Neira, M.: A passive reflectometry and interferometry system (PARIS): application to ocean altimetry. ESA J. 17, 331–355 (1993).

[4]. Hong, Xuebao & Zhang, Bo & Geiger, Alain & Han, Mutian & Yang, Dongkai. (2021). GNSS Pseudo Interference Reflectometry for Ground-Based Soil Moisture Remote Sensing: Theory and Simulations. IEEE Geoscience and Remote Sensing Letters. PP. 1-5. 10.1109/LGRS.2021.3068347.

[5]. Larson, Kristine & Small, Eric. (2014). Normalized Microwave Reflection Index: A Vegetation Measurement Derived From GPS Networks. Selected Topics in Applied Earth Observations and Remote Sensing, IEEE Journal of. 7. 1501-1511. 10.1109/JSTARS.2014.2300116.

[6]. Larson, K.M., Gutmann, E.D., Zavorotny, V.U., Braun, J.J., Williams, M.W., Nievinski, F.G.: Can we measure snow depth with GPS receivers? Geophys. Res. Lett. 36, L17502 (2009)
[7]. Reinking, J.. (2016). GNSS-SNR water level estimation using global optimization based on interval analysis. Journal of Geodetic Science. 6. 10.1515/jogs-2016-0006.
[8]. Martin-Neira, M.: A passive reflectometry and interferometry system (PARIS): application to ocean altimetry. ESA J. 17, 331–355 (1993)
[9]. Belmonte Rivas, Maria. (2003). Study on GNSS Carrier Phase for Ocean Altimetry. 10.13140/2.1.1304.0009.
[10]. Wang, Xiaolei & Niu, Zijin & Chen, Shu & He, Xiufeng. (2021). A Correction Method of Height Variation Error Based on One SNR Arc Applied in GNSS–IR Sea-Level Retrieval. Remote Sensing. 14. 11. 10.3390/rs14010011.
[11]. Song, Minfeng & He, Xiufeng & Wang, Xiaolei & Zhou, Ye & Xu, Xueyong. (2019). Study on the Quality Control for Periodogram in the Determination of Water Level Using the GNSS-IR Technique. Sensors. 19. 4524. 10.3390/s19204524.
[12]. Peng, Dongju & Feng, Lujia & Larson, Kristine & Hill, Emma. (2021). Measuring Coastal Absolute Sea-Level Changes Using GNSS Interferometric Reflectometry. Remote Sensing. 13. 4319. 10.3390/rs13214319.
[13]. Dahl-Jensen, Trine & Andersen, Ole & Williams, Simon & Helm, Veit & Khan, Shfaqat. (2021). GNSS-IR Measurements of Inter Annual Sea Level Variations in Thule, Greenland from 2008–2019. Remote Sensing. 13. 5077. 10.3390/rs13245077.
[14]. Sun Xuezhi, Zheng Wei, Wu Fan, et al. Improving the iGNSS-R ocean altimetric precision based on the coherent integration time optimization model[J]. Remote Sensing, 2021, 13: 4715
[15]. Wang, X., Zhang, Q. & Zhang, S. Water levels measured with SNR using wavelet decomposition and Lomb–Scargle periodogram. *GPS Solut* **22**, 22 (2018). https://doi.org/10.1007/s10291-017-0684-8
[16]. Zhang, Shuangcheng & Liu, Kai & Liu, Qi & Zhang, Chenglong & Zhang, Qin & Nan, Yang. (2019). Tide Variation Monitoring based improved GNSS-MR by Empirical Mode Decomposition. Advances in Space Research. 63. 10.1016/j.asr.2019.01.046.
[17]. Hu, Yuan & Yuan, Xintai & Liu, Wei & Wickert, Jens & Jiang, Zhihao & Haas, Rüdiger. (2021). GNSS-IR Model of Sea Level Height Estimation Combining Variational Mode Decomposition. IEEE Journal of Selected Topics in Applied Earth Observations and Remote Sensing. PP. 1-1. 10.1109/JSTARS.2021.3118398.

Authors

JieLi received his Bachelor's Degree from the School of Electronic and Information Engineering at Harbin Institute of Technology, Harbin, China, in 2016. From 2016 to 2018, he worked with his Master's Degree in Communication and Information Engineering. From 2020, he started pursuing the Ph.D. degree in Communication and Information Systems at Beihang University, Beijing, China. His interest lies in the Global Navigation Satellite System Reflectometry (GNSS-R) application in land observation.

DongkaiYang was born in 1972, in China. He received his BSc. in Electronic Engineering from the North University of China, Taiyuan, China, in 1994, and his MSc. and PhD in Communication and Information Systems from Beihang University, Beijing, China, in 1997 and 2000, respectively. From 2001 to 2002, he was a Research Fellow with the Nanyang Technological University, Singapore. Since 2010, he has been a full-time professor at the School of Electronic and Information Engineering at Beihang University. His interests include the Global

Navigation Satellite System (GNSS) and its applications.

Feng Wang received his Bachelor's Degree from the School of Electronic and Information Engineering at Beihang University, Beijing, China, in 2012. From 2012 to 2014, he worked with his Master's Degree in Communication and Information Engineering. From 2014 to 2019, he began pursuing his PhD. Degree in Information and Signal Processing. In 2020, he started his postdoctoral work at the School of Electronic and Information Engineering, Beihang University. His interest lies in the Global Navigation Satellite System Reflectometry (GNSS-R) application in earth observation.

Jin Xing received his Bachelor’s Degree from the School of Information Engineering, China University of Geosciences, in Beijing, China, in 2016. From 2016 to 2019, he worked on his Master Degree in electronic and information engineering at Hainan University. Since 2019, he has been pursuing his PhD. Degree in Information and Signal Processing at Beihang University. His interests include GNSS-R applications in ocean observations

Journal of Global Positioning Systems (2023)
Vol 18, No. 2: 103-113
DOI: 10.5081/gps.18.2.103

Journal of Global Positioning Systems
2022
© CPGPS

Photorealistic simulation platform for autonomous landing of fixed-wing aircraft

1st Weili Xue
School of Electronic Information and Electrical Engineering
Shanghai Jiao Tong University
Shanghai, China
u201613306@sjtu.edu.cn

2nd Zhen Sun
School of Electronic Information and Electrical Engineering
Shanghai Jiao Tong University
Shanghai, China
zhensun@sjtu.edu.cn

3rd Kehui Ma
School of Electronic Information and Electrical Engineering
Shanghai Jiao Tong University
Shanghai, China
khma@stu.xidian.edu.cn

4th Ling Pei✉
School of Electronic Information and Electrical Engineering
Shanghai Jiao Tong University
Shanghai, China
ling.pei@sjtu.edu.cn

***Abstract*—To investigate the vision-based autonomous landing of fixed-wing aircraft, we propose a photorealistic simulation platform that leverages ROS, Unreal Engine, and Pixhawk 4. This platform adopts a software-in-the-loop model consisting of rendering, control, communication, and sensor modules. To achieve realistic rendering control, the seawater hydrodynamics and fixed-wing aircraft dynamics are modeled. Based on the platform, we create simulation scenarios under different weather and disturbance conditions for autonomous landing of the aircraft carrier. The platform solves the problem that datasets of related scenes are difficult to collect and experiments are difficult to carry out. To verify the developability of the platform, we design and implement a runway line feature point extraction method (vision-based pose estimation algorithm), and evaluate the performance of the method under various conditions. Experiments show that our software-in-the-loop platform enables vision-based algorithm verification and supports simulation research for the autonomous landing of fixed-wing aircraft.**

***Keywords*—Photorealistic, Simulation platform, Fixed-wing aircraft, Landing**

I. Introduction

The evolution of aircraft landing on ships has undergone various stages, starting with the Landing Signals Officer (LSO) method, followed by the implementation of optical landing aid systems and finally, the advent of all-weather landing systems. In the early days of naval aviation, the LSO method was utilized to guide aircraft during landing, however, this approach was limited in its applicability due to the high speed of aircraft during the landing process. The 1960s saw the introduction of the Fresnel Lens Optical Landing System (FLOLS), which continues to be in use today, however, its shortcoming lies in the limited penetration and visibility of the light during cloudy weather conditions. To address this issue, long-range optical landing aid system [1] [2] was developed in the 1990s that utilized the superior penetration and straightness of laser beams to provide the pilot with landing information from a greater distance. Simultaneously, the All Weather Carrier Landing System (AWCLS) with a higher degree of autonomy has also matured, with a precision tracking radar on the carrier deck serving as its core component. The precision tracking radar measures the aircraft's motion and uses predictive estimation methods, such as Kalman filtering and neural networks, to compensate for interferences signals, such as deck motion, and assist the pilot in completing the landing operation. Recently, to address the challenges posed by unknown or GNSS-rejected environments, and strong electronic interference, the landing scheme has evolved from relying on single sensors to utilizing a multi-sensor approach. Among these, vision-based landing schemes have garnered increased attention from researchers [3]. Vision-based autonomous landing involves the use of an airborne camera to acquire image information of the target and then, through image processing techniques, calculates the relative attitude of the aircraft and the deck. The calculated attitude information is then transmitted to the flight control system to complete the autonomous landing process. Vision-based autonomous landing offers advantages such as low cost [4], high autonomy [5], and rich information [6].

Several institutions have undertaken research on vision-based

Editor-In-Charge: Dr. Qian Sun

landing and achieved noteworthy results. McCarthy et al. [5] explored the feasibility of a vision-based landing scheme for autonomous control and feedback. Zhang et al. [6] proposed the use of airborne forward-looking camera-acquired images to extract various navigation information, such as attitude and position, through a significance analysis method based on spectral residuals. Long et al. [4] analyzed the benefits of vision-based landing from the perspectives of low cost and anti-jamming capabilities. Additionally, they also discussed the design considerations for integrating vision-based schemes with radar-based and other schemes for landing. There have also been numerous studies dedicated to enhancing the performance of algorithms for feature extraction and pose estimation during landing [7] [8]. However, due to the absence of the high-fidelity simulation platform, many of the current algorithms for autonomous landing on aircraft carriers have not been tested in a relatively realistic simulation environment. The landing datasets utilized for testing purposes often have limited views or lack images of the moving ocean, and are usually of a single type, precluding experimentation under varying weather and disturbance conditions. Thus, the development of a high-fidelity simulation platform would greatly benefit research into vision-based carrier landing. Based on the above considerations, the simulation platform for autonoumous landing must have the following requirements: (1) It should reflect the dynamic characteristics and environmental characteristics of a real aircraft carrier as much as possible. (2)It should support algorithm verification and be able to generate datasets in different environments, e.g, different weather and different disturbance conditions.

Based on the above motivation, we build a simulation platform for autonomous landing of fixed-wing aircraft that has near-realistic rendering and dynamic models. To achieve photorealism, we model the dynamics of seawater and fixed-wing aircraft. This dynamic modeling simplifies the calculation process and reduces the resource consumption of rendering scenes on the premise of ensuring simulation accuracy. The platform implements software-in-the-loop from sensor, communication, control, and rendering modules. Finally, we use the platform to make various datasets. Based on different trajectories and weather conditions, we carried out the runway line reconstruction method to achieve pose estimation.

One of the ideal trajectories of aircraft landing is shown in Figure 1.

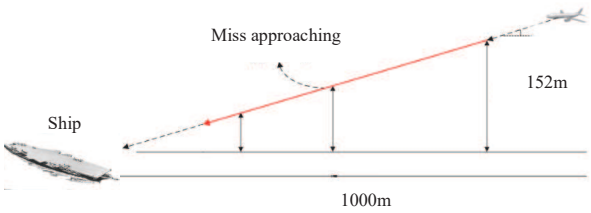

Fig. 1. Fixed-wing aircraft landing process diagram

The main contributions of our work are summarized as follows.

- We develop a photorealistic simulation platform for the autonomous landing of fixed-wing aircraft, which enables near-realistic rendering and dynamic models. This platform implements software-in-the-loop from sensor, communication, control, and rendering modules. We generate autonomous landing datasets under various weather(rain, fog) and disturbance conditions(random noise, horizontal noise lines) based on this platform.
- To model a photorealistic simulation scenario, we implement dynamic modeling for seawater and fixed-wing aircraft in the proposed platform. Meanwhile, our modeling considers the balance between photorealism and operational efficiency.
- With various experiments on our proposed platform, we demonstrate that the platform can be used to collect aircraft carrier landing datasets under various external conditions and support advanced algorithm development. This solves difficulties associated with datasets creation and simulation experiments in the field of fixed-wing landing on aircraft carrier.

The remainder of this paper is organized as follows: Section II introduces related work in the field of simulation platforms, seawater dynamics modeling and pose estimation. Section III introduces the architecture of the proposed simulation platform. Section IV introduces the dynamic modeling and implementation of seawater and fixed-wing aircraft. Section V introduces the runway line reconstruction method. Section VI describes the experimental portion of the study. Section VII summarizes our work and proposes future work.

II. Related Work

Aircraft simulation platform. Due to their excellent developability, most simulation platforms are based on ROS using Linux systems [9] [10] [11]. Tim et al. [12]developed a fixed-wing simulation platform. It is a classic project often used to teach novice engineers how to develop drone simulation platforms. However, it lacks the implementation of high-level algorithms. Xiao et al. [13]implemented a powerful UAV simulation platform XTDrone which is based on ROS and PX4. This platform supports SLAM algorithms such as VIO, as well as multi-UAV path planning. However, Gazebo's rendering falls short of photorealism. Shital Shah [14] et al. completed a great simulation platform AirSim, which combines the excellent visualization capability of Unreal Engine with its own dynamics and control system. However, AirSim is not suitable for all scenarios due to its limited vehicle and drone models. For example, it only supports quadrotor aircraft and does not implement a fixed-wing dynamic model. Integrating the previous work, we complete a photorealistic simulation platform for the autonomous landing of fixed-wing aircraft.

Dynamics modeling. In the field of sea surface dynamics modeling, modeling and animating the ocean's surface, mainly

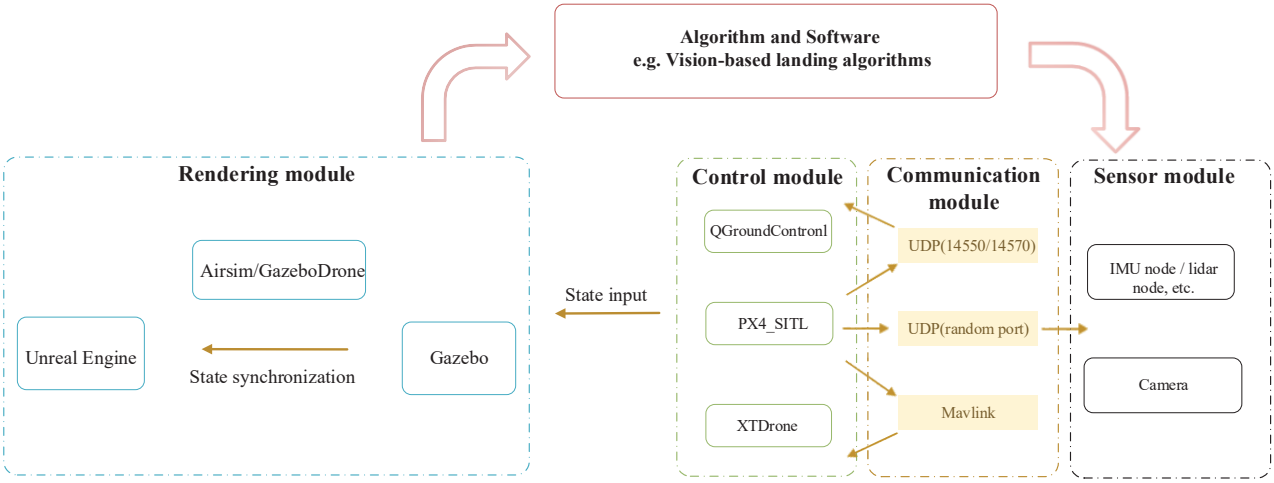

Fig. 2. Platform architecture

TABLE I
DISPLAY FORM OF AIRCRAFT CARRIER LANDING PLATFORM SUPPORT FUNCTIONS

Weather simulation	Interference simulation	Customizable dynamics model	Track control	Supported sensors
rain, fog, snow	random, horizontal	fixed-wing, quadrotor	real-time, pre-planning	camera, IMU

1 Random is Gaussian random noise. The pixels in a unit area share the same noise value that satisfies the Gaussian random distribution.
2 Horizontal is the horizontal noise line. The horizontal noise lines increase the noise area on the horizontal line.
3 The fixed-wing dynamic model has now implemented the Cessna C-172.
4 Real-time track control relies on the keyboard. Meanwhile, the pre-planning of trajectories relies on QGroundContronl.

rely on two approaches: 1) the approximation of ocean dynamics with parametric, spectral or hybrid models and the use of empirical laws from oceanographic research. and 2) physics-based methods that use Navier–Stokes equations to represent breaking waves and, more generally, ocean surfaces near the shore. For example, Mark et al. [15] proposes different models for global ocean modeling at different resolution requirements. The model can simulate climate change and eddy current activity. However, it cannot be used for rendering pipelines and simulation scenes due to their computational complexity. Considering the balance between photorealism and operational efficiency, we decided to use the sea surface height function [16] to simulate the ocean surface and ship motion. In the field of fixed-wing dynamics modeling, there are many mature theories and models. We chose the most classic one, Cessna C-172 [17]

III. Simulation Platform

In this section, we first describe the structure of the platform. Then, we introduce the modules that make up the platform in detail, such as the rendering module, control and communication module, and sensor module.

A. Platform architecture

Table I shows the functions currently supported by our platform. Figure 2 shows the detailed architecture of the simulation platform. The platform contains rendering, communication, control, and sensor modules. Among them, the communication module mainly uses the Mavlink protocol and topic communication. The bottom layer motor of the control module is simulated by PX4_SITL, and the upper QGroundControl is used to plan the flight path of the aircraft. XTDrone is used for SLAM algorithm development. The aircraft flight status is sent to Gazebo for display. The rendering module reads the aircraft states from Gazebo and synchronously displays them in the scene simulated in Unreal Engine. The sensor module mainly includes the camera. The platform can feed back the pose information of the sensor module to the rendering module through the control and communication module. The above modules construct a software-in-the-loop pipeline.

B. Rendering module

1) Rendering in Unreal Engine: Modern visual engines, such as Unreal Engine, exhibit far better visual performance than Gazebo, which is used for robot simulation display on the Linux platform. An important reason is that the former realizes ray tracing and physics-based rendering. We are able to sculpt realistic models in professional modeling software such as Blender. We can provide normal maps, specular maps, and noise maps to render models and obtain near-realistic materials [18].

C. Control and communication module

The underlying flight control and dynamics model are implemented based on PX4. The upper-layer communication scripts, control algorithms, and state estimation are implemented by XTdrone. The communication between the aircraft and the

simulation scene in Gazebo is realized through the Mavros module of ROS. Topic communication is used between nodes, and the specific message format can refer to [13]. At the same time, we realize point-to-point flight control and modification of flight parameters through QGroundControl.

D. Sensor module

A real camera has many parameters, such as external parameters, internal parameters, and distortion. Therefore, the parameters of the simulated camera used by the platform are similar. The internal parameters of the camera are:

$$f_x = f_y = \frac{Width/2}{tan(fov/2)} \tag{1}$$

$$K = \begin{bmatrix} f_x & 0 & \frac{Width}{2} \\ 0 & f_y & \frac{High}{2} \\ 0 & 0 & 1 \end{bmatrix} \tag{2}$$

In the formula, *width* and *high* are the length and width of the photo, and *fov* is the camera field of view.

The camera distortion parameters default to 0, which can be customized in [14].

IV. Dynamics Modeling

In this section, we introduce the principles and implementation of seawater dynamics modeling and fixed-wing dynamics modeling. The state variables used in the derivation process can be found in Table II.

TABLE II
THE VARIABLES USED IN THE DERIVATION PROCESS

Variables	Description
ρ, u, p	Fluid density, fluid velocity and pressure
μ, ϕ, g	Fluid viscosity, velocity potential, gravitational acceleration
U	$U = gh$ is the gravitational potential of the fluid h is the sea level
k	The wave vector, which points in the direction of the motion of the wave, $k = \frac{2\pi}{\lambda}$, λ is wavelength
ι	$\iota = \frac{v^2}{g}$,v is the wind speed
ω, w, A	Angular frequency, wind direction, seawater amplitude
θ	θ is theangle between wave vector and wind direction
F^i	Inertial coordinate system(North-East-Down)
F^v	Aircraft coordinate system as Figure 3(a)
F^{v1}	Aircraft-1 coordinate system as Figure 3(b). The F^{v1} coordinate system is obtained by rotating F^v coordinate system around the K^v-axis by an angle ψ
F^{v2}	Aircraft-2 coordinate system as Figure 3(c). The F^{v2} coordinate system is obtained by rotating F^{v1} coordinate system around the j^{v1}-axis by an angle θ
F^b	Body coordinate system as Figure 3(d)
P_n, P_e, P_d	The inertial north, east, down of the MAV along the i^i, j^i, k^i axis in the F^i coordinate system
u, v, w	velocity along i^b, j^b, k^b axis in F^bcoordinate system
ϕ, θ, φ	Roll, Pitch, Yaw angle
p, q, r	Roll, Pitch, Yaw velocity along the i^b, j^b,k^b axis in the F^bcoordinate system

A. Seawater hydrodynamic modeling

In the selected scene, the datasets images are mostly images of the ocean, so it is important to render high-fidelity seawater. We make the following assumptions:(1) Seawater is an incompressible fluid. (2) The current of seawater does not cross. (3) The density of seawater is constant. (4) Turbulence is ignored. From the Navier-Stokes equation and the fluid continuity equation, under the above assumptions, the mass conservation and momentum conservation constraints of seawater can be obtained:

$$\begin{cases} \frac{\partial \phi}{\partial t} + \frac{1}{2}(\bigtriangledown \phi)^2 = -U - p \\ \bigtriangledown^2 \phi = 0 \end{cases} \tag{3}$$

According to plane wave theory and substituting into the directional wave spectrum (Philippe spectrum), combined with the empirical formula of ocean statistics [19], the approximate solution of the sea surface height can be obtained:

$$h(x,t) = \sqrt{\frac{A}{2}}(\varepsilon_r + i\varepsilon_i)\sum_k \frac{|k \cdot w|}{k^2} e^{\frac{i}{k\iota}} \tag{4}$$

where x are sea level coordinates and $\varepsilon_i, \varepsilon_r \sim N(0,1)$ are normally distributed random numbers. For a more detailed proof of the seawater height function, refer to [16]. Then, we use the height function in Unreal Engine to simulate fluctuating sea surface.

B. Fixed-wing aircraft dynamics modeling

The coordinate systems we used are shown in Figure 3, in which Figure 3(e) shows the definition of the aircraft motion axis. For fixed-wing aircraft, the dynamic system is highly relative to the control system.

There is a relationship of :

$R_v^b(\varphi,\theta,\psi) = R_{v1}^b(\varphi)R_{v1}^{v2}(\theta)R_b^{v1}(\psi)$, and the transformation matrix from the aircraft coordinate system F^v to the body coordinate system F^b is:

$$R_v^b(\varphi,\theta,\psi) = \begin{bmatrix} c_\theta c_\psi & c_\theta s_\psi & -s_\theta \\ s_\varphi s_\theta c_\psi - c_\varphi s_\psi & s_\varphi s_\theta s_\psi - c_\theta c_\psi & s_\varphi c_\theta \\ c_\theta s_\theta c_\psi + s_\varphi s_\psi & c_\varphi s_\theta s_\psi - s_\varphi c_\psi & c_\varphi c_\theta \end{bmatrix} \tag{5}$$

By linking the translation velocity and position, the constraints of position can be obtained:

$$\frac{\mathrm{d}}{\mathrm{d}t}\begin{bmatrix} P_n \\ P_e \\ P_d \end{bmatrix} = (R_v^b)^T \begin{bmatrix} u \\ v \\ w \end{bmatrix} \tag{6}$$

When the plane is performing translational motion, combined with Newton's second law, the force and velocity in body coordinates, as shown in Figure 3(d) can be expressed as:

$$m(\frac{\mathrm{dV_g^b}}{\mathrm{d}t_b} + \omega_{b/i}^b \times V_g^b) = f^b \tag{7}$$

where $V_g^b = (u,v,w)^T$,$\omega_{b/i}^b = (p,q,r)^T$.

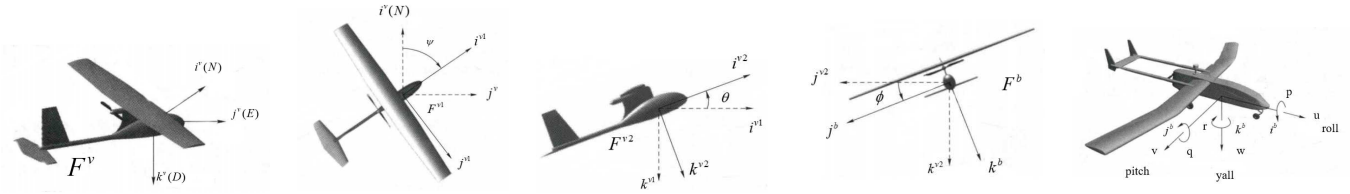

(a) aircraft coordinate (b) aircraft-1 coordinate (c) aircraft-2 coordinate (d) body coordinate (e) motion axis

Fig. 3. Definition of the coordinate systems

and $f^b = (f_x, f_y, f_z)^T$ represents the sum of all external forces in the body coordinate system. After substituting Formula (7) for simplification, we can obtain the velocity constraints:

$$\frac{\mathrm{d}}{\mathrm{d}t}\begin{bmatrix} u \\ v \\ w \end{bmatrix} = \begin{bmatrix} rv - qw \\ pw - ru \\ qu - pv \end{bmatrix} + \frac{1}{m}\begin{bmatrix} f_x \\ f_y \\ f_z \end{bmatrix} \tag{8}$$

In the same way, combined with the angular momentum and angular velocity projection, the constraint of the aircraft's rotational motion can be obtained as:

$$\frac{\mathrm{d}}{\mathrm{d}t}\begin{bmatrix} p \\ q \\ r \end{bmatrix} = \begin{bmatrix} \Gamma_1 pq - \Gamma_2 qr + \Gamma_3 l + \Gamma_4 n \\ \Gamma_5 pr - \Gamma_6 (p^2 - r^2) + \frac{m}{J_y} \\ \Gamma_7 pq - \Gamma_1 qr + \Gamma_4 l + \Gamma_8 n \end{bmatrix} \tag{9}$$

where:

$$\begin{cases} \Gamma_1 = \frac{J_{xz}(J_x - J_y + J_z)}{\Gamma}, \Gamma_2 = \frac{J_z(J_z - J_y) + J_{xz}^2}{\Gamma} \\ \Gamma_3 = \frac{J_z}{\Gamma}, \Gamma_4 = \frac{J_{xz}}{\Gamma}, \Gamma_5 = \frac{J_z - J_x}{J_y} \\ \Gamma_6 = \frac{J_{xz}}{J_y}, \Gamma_7 = \frac{(J_x - J_y)J_x + Jxz^2}{\Gamma}, \Gamma_8 = \frac{J_x}{\Gamma} \\ \Gamma = J_x J_z - J_{xz}^2 \end{cases} \tag{10}$$

and:

$$J = \begin{bmatrix} J_x & -J_{xy} & -J_{xz} \\ -J_{xy} & J_y & -J_{yz} \\ -J_{xz} & -J_{yz} & J_z \end{bmatrix} \tag{11}$$

where J is the rotational inertia matrix of the aircraft, in which the diagonal elements J_x, J_y, J_z are inertial momentum, and the off-diagonal elements are inertial products. The above equations (6)(8)(9) give the fixed-wing aircraft's kinematic and dynamic constraints of 6-DOF and 12-states, respectively. The detailed derivation process can be found in [12]. Numerical solvers that simulate rigid body dynamics use the open dynamics engine(ODE) [20].

V. Vision-Based Pose Estimation Algorithm for Platform Verification

In this section, we first introduce the algorithm pipline for estimating the aircraft attitude in the fixed-wing landing scenario. Next, we briefly describe the implementation details and code of the algorithm.

A. Method and algorithm pipeline

The pipeline design of our method is shown in Figure 4. First we need a target detection algorithm to process the image frames of the datasets to obtain the region of interest (ROI) of the aircraft carrier. In view of the requirement for real-time operation during the landing process, the target detection of the first step of the algorithm must not drag down performance. The simulation environment utilized in this study has a rendering pipeline established in Unreal Engine, yielding a maximum output frame rate of 60 frames per second (FPS). As a result, it is necessary to select a target detection algorithm with sufficient operational efficiency, specifically, a rate greater than 60 FPS. After conducting a thorough evaluation, YOLOv5 is deemed an appropriate choice, as it has a maximum frame rate of 140 FPS and demonstrate satisfactory performance in detecting small targets. Next, we binarize the ROI and perform edge detection and corner extraction on the binary image. Then, we use a priori infomation to obtain the priori region of the runway line and use this region to filter out the corner points. Finally, we use the corner points to reconstruct the new runway line, find the endpoints, and run the Perspective-n-Point algorithm [21] to determine the pose estimation. The algorithm pipeline is shown in Algorithm 1.

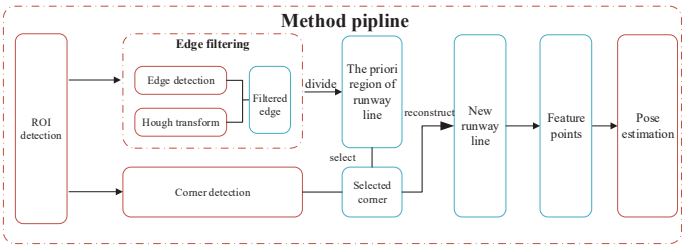

Fig. 4. Pipeline of the proposed method

B. Details of the algorithm

After we obtain the region of interest(ROI) of the airport runway, we also get the pixel height and width of the aircraft carrier in the picture, which are recorded as *Height* and *Width*. After preliminary experiments, we find that due to blurry pictures in the ROI area and many interference lines, the edge detection has the following problems: (1) The detected runway edge is not a complete straight line but is instead composed of multiple small line segments oriented in slightly different directions; (2) the edges of other parts of the carrier can also

Algorithm 1: Method pipeline

Data: *datasets* collected based on the platform
Result: Pose of Euler Angles
while *1 in all frames* **do**
  `// In this example we use YOLOv5`
  Object Detection;
  threshold() and medianBlur();
  Canny() HoughLinesP();
  SelectEdge() and SetArea();
  img = cornerHarris();
  Normalize();
  for *pixel in img* **do**
    if *(pixel.color* $>$ *threshold* ***and*** *is_inarea(*pixel*)* *== True)* **then**
      add pixel to Points[];
    end
  end
  `// New runway line fitting`
  Reconstruction::RANSAC(Points[]);
  `// Pose estimation`
  SolvePnP();
end

be detected, which introduces noise to the runway line edge detection. Based on the above facts, we decided to jointly use Canny [22] operator edge detection, Hough Transform [23], and Harris corner detection [24].

The constraints we use to filter runway lines are:

$$\begin{cases} \theta \epsilon (\theta_{min}, \theta_{max}) \\ L \epsilon (L_{min}, L_{max}) \end{cases} \tag{12}$$

As shown in Formula (12), θ is the horizontal angle of the line, where θ_{min} and θ_{max} are the angle ranges of the aircraft carrier runway line under the current trajectory. L is the length of the line, where L_{max} is the maximum length. According to the runway line length of the real model of the aircraft carrier, $L_{max} = 0.6 * Width$ (*Width* is the width of the ROI), and L_{min} is the minimum length of the edge line. We take a empirical value for the minimum length. For each edge of the runway line chosen, we establish a rectangle where the rectangle is oriented along the direction of the edge. The ideal runway area can be obtained by superimposing all rectangles. This step is shown in Figure 5.

C. Runway line reconstruction

We use a priori region, which is shown in Figure 5, to filter corners and group them into sets $\{S_a\}, \{S_b\}$. Then we use the RANSAC algorithm to mitigate the outliers.As long as the new runway line is constructed, we also obtain the endpoints of the runway line. We denote these endpoints as P_0, P_1, P_2, P_3. Because the camera intrinsic matrix K is known, the real coordinates and the accurate pixel coordinates

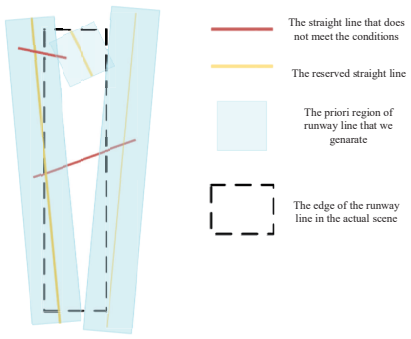

Fig. 5. Edge selection and runway division

of the four points P_0, P_1, P_2, P_3 are also known, and we apply the Perspective-n-Point algorithm to estimate the camera pose.

VI. Experiments

In this section, we first introduce the software and hardware configuration. Then, we show the details of the simulation environment construction. Next, we describe the experimental steps of the algorithm. Furthermore, we conduct experiments under different weather conditions and trajectories and evaluate the performance of the algorithm in different situations. This demonstrates that our platform can support experiments under a variety of conditions and further supports algorithm development and verification.

A. Configuration

1) Software: The software environment is Ubuntu 18.04, Python version 3.7.2, AirSim version 1.7.0 [14], Unreal Engine 4.25 [25], ROS-neotic [26],PX4, Gazebo9.1, QGroundControl, and XTDrone [13].
2) Hardware: The hardware equipment used in this experiment includes an Nvidia RTX2060 GPU and an Intel(R) Core(TM) i7-10875H CPU @ 2.30GHz.

B. Construction details of the aircraft carrier fixed-wing landing environment

In this section, we briefly describe the simulation environment components.
1) Construction of a photorealistic sea: Using the height function in formula 4, we can generate the height spectrum in Unreal Engine and then obtain the offset spectrum. Knowing the offset spectrum, we implement IFFT to obtain the (x, y, z) offset. The offset is superimposed to obtain the offset texture and then the normal texture can be calculated through the offset texture. Finally, we use the normal texture for rendering. This process is shown in Figure 6. Considering the aircraft carrier as a rigid body with a center of mass, and assigning the offset in the Z direction of one point to the center of mass, the vibration of the aircraft carrier deck at sea can be roughly simulated. In addition, to get the photorealistic seawater in Unreal Engine, we also need to set the water depth, caustics, and foam. The final built sea surface is ideal (without shoals, edges, and rapids), as shown in Figure 7.

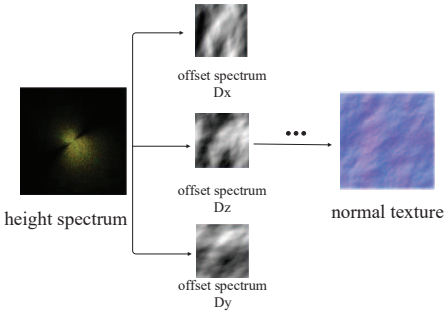

Fig. 6. Normal texture of the generated seawater

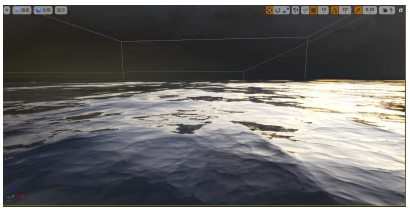

Fig. 7. Ideal sea rendering in Unreal Engine

2) Other details of the aircraft carrier fixed-wing landing environment: The prototype of the aircraft carrier used in the simulation is the Nimitz Class Aircraft Carrier, as shown in figure 8(a). The fighter prototype used for landing is the Lockheed Martin F-35 Lightning II, as shown in Figure 8(b). In addition, to simplify the experiment, for the fixed-wing dynamic model we temporarily use the Cessna C-172.

(a) Nimitz Class Aircraft Carrier (b) Lockheed Martin F-35 Lightning

Fig. 8. Aircraft carrier and fixed-wing aircraft prototype display

3) The trade-off between photorealism and operational efficiency: Datasets rendering supports various resolutions (360P, 480P, 1080P, 2K, 4K). The higher the resolution is, the higher the computing power required for rendering. The relatively simple dynamic modeling of the sea surface and fixed wings can significantly reduce the computing power requirements for rendering and improve the frame rate performance, but it will lose the realism of the picture. Table III shows the relationship between the frame rate and resolution under the current experimental environment. In this table, we compare our platform's fixed-wing landing scenario, the default scenario in Gazebo, and the Airsim scenario based on our platform with the fixed-wing dynamics removed. Obviously, compared to Gazebo, we sacrifice operating efficiency for the improvement of photorealism. At the same time, the frame rate of our platform is not much different from that of native AirSim at high resolution. This means that the platform achieves the need for a customizable fixed-wing dynamic model without sacrificing operational efficiency. In addition, the frame rate performance of the current environment at high resolution (1080P) can meet most of the experimental requirements.

TABLE III
THE FRAME RATE PERFORMANCE OF OUR ENVIRONMENT UNDER DIFFERENT RESOLUTION REQUIREMENTS

Resolution	480P	720P	1080P	2K	No-re	Fixed-wing
Ours	39	34	15	7	20	✓
Gazebo	100+	84	67	NULL	60	✓
Airsim	41	36	16	7	23	✘

1 The unit of frame rate is FPS. When rendering the datasets, the environment is not displayed in real time.
2 No-re refers to the frame rate at which the platform is running without rendering the datasets.
3 NULL indicates that the current scene cannot perfectly support the condition.

C. Vision-based pose estimation algorithm implementation

In this part, we control the fixed-wing aircraft to fly a fixed trajectory in QGroundControl and generate datasets. Subsequently, we implement our algorithms based on the above datasets and analyze the results of the experiment.

1) Flight demonstration: We show the entire process of a fixed-wing aircraft from take-off to landing along a fixed trajectory in a demo video. The flight trajectory is controlled by QGroundControl. The coordinates of the ideal flight landing point in the Unreal Engine world scene are (0, 0, 24.3) (the above coordinate units have been converted to meters). Figure 9(a) shows the trajectory of the aircraft. The landing algorithm uses the PX4 default method AUTO_LAND. The dynamic of the fixed-wing aircraft uses the classic Cessna C-172 [27]. Figure 9(b) shows the flight demonstration with the depth image, camera image and semantic segmentation image.

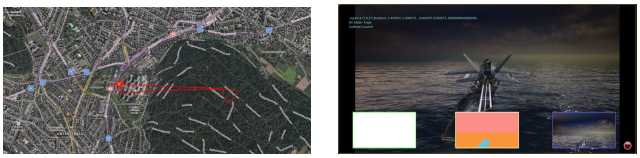

(a) QGroundControl (b) Unreal Engine

Fig. 9. The trajectory shown in QGroundControl and the corresponding flight process in Unreal Engine

2) Datasets generation: For the multiconditional experiments in the next section, we generate datasets of fixed-wing aircraft landings on the deck of an aircraft carrier under different trajectories, weather(rain, fog) and interference conditions (random noise, horizon noise lines), as shown in Table IV.

3) Vision-based pose estimation algorithm: Figure 10 shows the complete pipeline for runway line feature extraction. Considering the layout space, the pictures, except for Figure 10(a) , only show the region of interest. Among them, Figure 10(a) is the YOLO recognition result, Figure 10(b) is the binarized image, Figure 10(c) is the result of the edge detection and Figure 10(d) is the line detection based on the edge detection

TABLE IV
THE FORMAT OF THE DATASETS CONFIGURATION

Size	TimeStamp	*POS_X*	*POS_Y*	*POS_Z*
210	168988397609	5.27	-1.945	-9.99
Q_W	*Q_X*	*Q_Y*	*Q_Z*	Condition
-0.02542	0.02811	0.001381	-0.999	rain, fog, noise

image. Figure 10(e) is the corner detection result, the red dots are the points used for RANSAC. Figure 10(f) is the runway line fitting result. The algorithms effectively extract the features of the runway line in the distance.

(a) region of interest

(b) (c) (d) (e) (f)

Fig. 10. The whole process of runway line feature extraction using the vision-based pose estimation algorithm

4) Pose estimation: Based on the extracted feature points with known world coordinates and pixel coordinates, we run the Perspective-n-Point algorithm. We compare the pose estimation and the ground truth in pitch, roll, and yaw in Figure 11. When the aircraft is diving and descending towards the aircraft carrier, the error in the pitch and roll directions is between 5 degrees, but the error in the yaw direction is higher than 10 degrees. At the same time, as time progresses, as the aircraft approaches the aircraft carrier, the error of pose estimation tends to decrease. Obviously, it can be seen that the trend of the curve is consistent with the ground truth, which indicates that the feature points we extracted are valid. However, our method for pose estimation has better performance in the near space, but the accuracy decreases in the distance. This is because the Perspective-n-Point algorithm is not sufficiently accurate with fewer points, and we do not utilize multisensor fusion to design feedback for the elimination of errors.

D. Vision-based pose estimation algorithm under various conditions

We design two different flight trajectories. The landing points of both trajectories are (0, 0, 24.3). The first trajectory lands directly on the aircraft carrier, and the start recording point is (0,1000, 153), while the second trajectory lands on the side of the aircraft carrier, and the start recording point is (200, 1000, 153). Table V shows the performance of the algorithm under different weather conditions(normal, rain, fog), different interference conditions (normal, random noise, horizontal noise lines), and different trajectories (trajectory I, trajectory II). The criteria P_s, Δ_{error} for evaluating the quality of feature point extraction follow the formula:

$$\begin{cases} P_s = N_s/N \\ \Delta_{error} = \frac{1}{n}\sum_i^n \sqrt{(x_i - x)^2 + (y_i - y)^2} \end{cases} \tag{13}$$

where N_s is the number of datasets from which feature points are successfully extracted, and N is the size of the datasets. Meanwhile, (x_i, y_i) are the pixel coordinates of the extracted feature points, and (x, y) are their corresponding real pixel coordinates. n is the set of extracted feature points. Furthermore, we present a set of representative recognition images in Fig 12 to show the influence of different external conditions on the algorithm.

TABLE V
PERFORMANCE OF THE ALGORITHM UNDER DIFFERENT CONDITIONS

Trajectory	*Weather*	*Interference*	P_s	Δ_{error}	Degree
I(facing)	normal	normal	0.829	5.23	0
I(facing)	normal	**random**	0.814	35.9	3
I(facing)	normal	**horizontal**	0.819	24.2	2
I(facing)	**rain**	normal	0.543	7.93	2
I(facing)	**fog**	normal	0.362	17.7	4
II(oblique)	normal	normal	0.733	12.4	1
II(oblique)	normal	**random**	0.700	44.7	4
II(oblique)	normal	**horizontal**	0.719	39.9	3
II(oblique)	**rain**	normal	0.476	18.6	3
II(oblique)	**fog**	normal	0.333	22.5	5

1 In Trajectory I, the aircraft is facing the aircraft carrier. While, the aircraft in trajectory II is on the oblique side of the aircraft carrier.
2 P_s represents the runway feature points extraction success rate.
3 Δ_{error} represents the feature point average pixel error.
4 normal is the ideal situation with no weather disturbances or noise.
5 Random is Gaussian random noise. Random noise is Gaussian random noise. The pixels in a unit area share the same noise value that satisfies the Gaussian random distribution.
6 Horizontal is the horizontal noise line. The horizontal noise lines increase the noise area on the horizontal line.
7 Degree is a qualitative reference compared to ideal, describing the effect of trajectory, weather, noise, etc. on algorithm performance. Degree is divided into 5 levels from 0 to 5.

The results in Table V and Fig 12 show that the trajectory, simulated weather, and interference noise all affect the extraction of runway line feature points for the algorithm. From the perspective of weather, in rainy conditions, raindrops block the target, which reduces the success rate of feature point extraction, but the accuracy of point extraction is not affected. However, in foggy weather, the visibility in the environment is reduced, which has a great impact on both target detection and feature point extraction. Next, from the perspective of noise, under random noise conditions, the picture distortion is serious, and the success rate of feature point extraction remains unchanged, but the accuracy is greatly reduced. Compared with random noise, the horizontal noise lines perform better because the noise only exists in the horizontal direction. In addition, due to the threshold setting inside the algorithm, the different trajectories selected will also affect the performance of the algorithm.

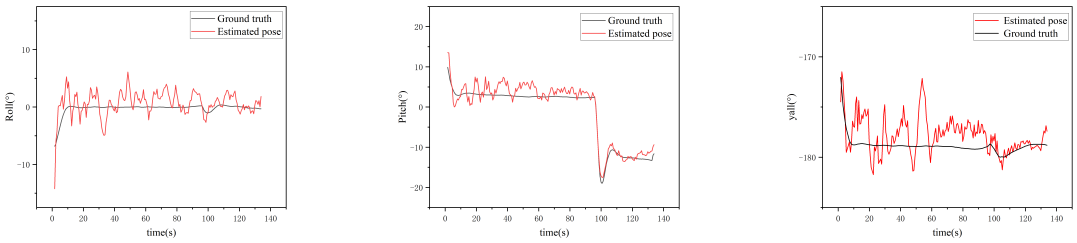

(a) Ground truth *vs* estimated pose in roll (b) Ground truth *vs* estimated pose in pitch (c) Ground truth *vs* estimated pose in yaw

Fig. 11. Comparison of the pose estimation results under three rotation angles

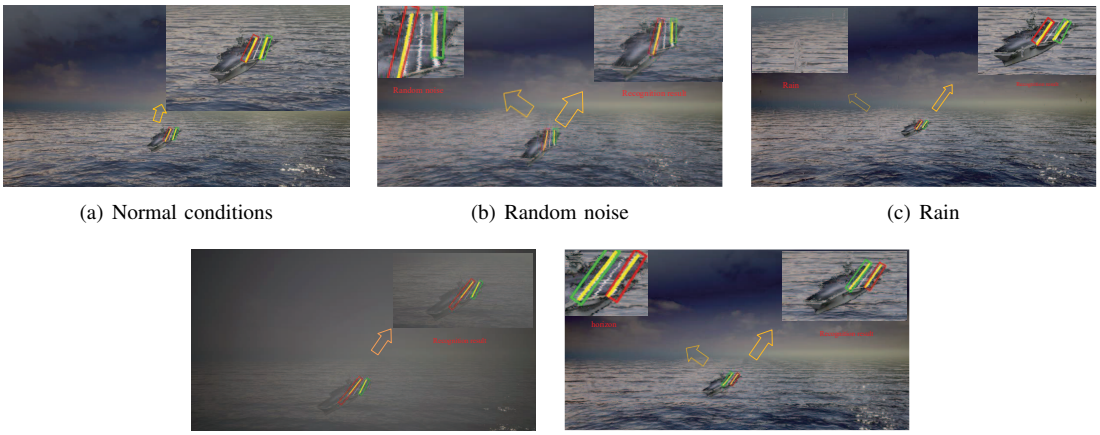

(a) Normal conditions (b) Random noise (c) Rain

(d) Fog (e) Horizon noise lines

Fig. 12. The performance of the algorithm under different conditions

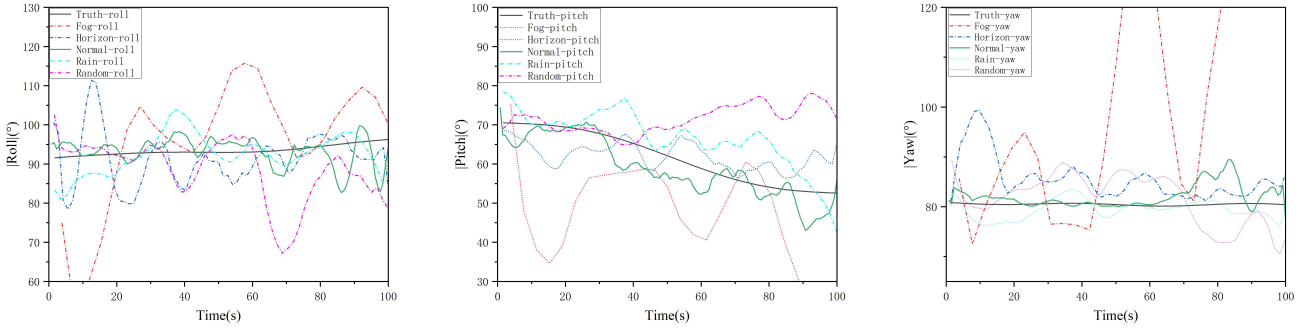

Fig. 13. Pose estimation results for various situations in trajectory II

The figure 13 demonstrates the aircraft carrier landing pose estimation results in trajectory II (To facilitate analysis, we apply mean filtering to the pose estimation results). The pose estimation results are compared under different interference scenarios, including normal, foggy, rainy, horizontal noise, and random noise. It is observed that the accuracy of feature point extraction significantly impacts the accuracy of the pose estimation results. Under normal conditions, where the feature point extraction accuracy is high, the pose estimation results are in good agreement with the ground truth value. Conversely, in foggy weather conditions with the lowest extraction accuracy of feature points, the pose estimation results deviate the most. Furthermore,Table VI displays the absolute error of the pose estimation results in each direction. When the accuracy of feature point extraction is low, the results of pose estimation will lose their reference significance. Hence, to improve the accuracy of pose estimation, it is recommended to use more feature points to solve the pose and select a better pose estimation algorithm.

Thus far, we have completed the design, implementation, and evaluation of the vision-based pose estimation algorithm on the photorealistic simulation platform.

TABLE VI
POSE ESTIMATION ERROR FOR VARIOUS SITUATION

Trajectory	*Weather*	*Interference*	Δin Roll	Δin Pitch	Δin Yaw
II	normal	normal	4.23	6.91	2.64
II	normal	**random**	12.78	17.23	7.33
II	normal	**horizontal**	8.44	9.14	9.61
II	**rain**	normal	4.55	7.44	3.95
II	**fog**	normal	23.11	34.61	45.89

1 This table provides a complementary error analysis of the pose estimation results presented in Figure 13.
2 The dataset used for test comprises 150 frames.
3 Δ denotes the average of the absolute error between the estimated and true attitude values.

VII. CONCLUSION AND FUTURE WORK

In this paper, we develop a photorealistic simulation platform for the autonomous landing of fixed-wing aircraft, which has near-realistic rendering and dynamic models. The platform solves the problems that the aircraft carrier deck landing datasets is difficult to produce and advanced experiments are difficult to carry out. At the same time, by testing algorithms under various conditions, we show that our software-in-the-loop platform can be used for algorithm verification and advanced development. We share demo videos and datasets datasets at https://github.com/U201613306/flight-demonstration.git

In future work, we plan to further enhance the platform by incorporating additional sensor simulations onto the existing infrastructure. Additionally, we intend to design a multi-sensor fusion experiment [28] in order to evaluate the functionality of the simulation module. At present, the simulation of the sea surface on the platform does not take into account the impact of sea conditions. As a result, we aim to simulate typical sea conditions by incorporating noise maps into the simulation.

ACKNOWLEDGMENT

This work is supported by the Equipment Pre-Research Field Foundation under Grant 80913010303.

REFERENCES

[1] William Lee Wellons. *A shipboard global positioning system carrier phase interferometric aircraft flight reference system*. PhD thesis, Ohio University, 1994.

[2] Alison Brown and B Matthews. A robust gps/ins kinematic integrity algorithm for aircraft landing. In *Proceedings of the 19th International Technical Meeting of the Satellite Division of The Institute of Navigation (ION GNSS 2006)*, pages 715–725, 2006.

[3] Dengqing Tang, Tianjiang Hu, Lincheng Shen, Daibing Zhang, Weiwei Kong, and Kin Huat Low. Ground stereo vision-based navigation for autonomous take-off and landing of uavs: a chan-vese model approach. *International Journal of Advanced Robotic Systems*, 13(2):67, 2016.

[4] Long Xin, Zimu Tang, Weiqi Gai, and Haobo Liu. Vision-based autonomous landing for the uav: A review. *Aerospace*, 9(11):634, 2022.

[5] Tyler B McCarthy. Feasibility study of a vision-based landing system for unmanned fixed-wing aircraft. Technical report, Naval Postgraduate School Monterey United States, 2017.

[6] Zhouyu Zhang, Yunfeng Cao, Meng Ding, Likui Zhuang, and Jiang Tao. Vision-based guidance for fixed-wing unmanned aerial vehicle autonomous carrier landing. *Proceedings of the Institution of Mechanical Engineers, Part G: Journal of Aerospace Engineering*, 233(8):2894–2913, 2019.

[7] XiaoBin Xu, Zhao Wang, and YiMin Deng. A software platform for vision-based uav autonomous landing guidance based on markers estimation. *Science China Technological Sciences*, 62:1825–1836, 2019.

[8] Zhuo Zhang, Qing Shi, Hui Huang, and Xiaoliang Sun. Application of centernet technology in the process of shipborne aircraft autonomous landing. In *2022 5th International Symposium on Autonomous Systems (ISAS)*, pages 1–6. IEEE, 2022.

[9] Yifan Zhu, Ling Pei, Danping Zou, Wenxian Yu, Tao Li, Qi Wu, and Songpengcheng Xia. A geometric consistency model of virtual camera for vision-based slam simulation. In *International Conference on Spatial Data and Intelligence*, pages 271–280. Springer, 2020.

[10] Xinglong Yang, Danping Zou, Ling Pei, Daniele Sartori, and Wenxian Yu. An efficient simulation platform for testing and validating autonomous navigation algorithms for multi-rotor uavs based on unreal engine. In *China Satellite Navigation Conference*, pages 527–539. Springer, 2019.

[11] Rongzhi Wang, Danping Zou, Changqing Xu, Ling Pei, Peilin Liu, and Wenxian Yu. An aerodynamic model-aided state estimator for multi-rotor uavs. In *2017 IEEE/RSJ International Conference on Intelligent Robots and Systems (IROS)*, pages 2164–2170. IEEE, 2017.

[12] Gary Ellingson and Tim McLain. Rosplane: Fixed-wing autopilot for education and research. In *2017 International Conference on Unmanned Aircraft Systems (ICUAS)*, pages 1503–1507. IEEE, 2017.

[13] Kun Xiao, Shaochang Tan, Guohui Wang, Xueyan An, Xiang Wang, and Xiangke Wang. Xtdrone: A customizable multi-rotor uavs simulation platform. In *2020 4th International Conference on Robotics and Automation Sciences (ICRAS)*, pages 55–61. IEEE, 2020.

[14] Shital Shah, Debadeepta Dey, Chris Lovett, and Ashish Kapoor. Airsim: High-fidelity visual and physical simulation for autonomous vehicles. In *Field and service robotics*, pages 621–635. Springer, 2018.

[15] Todd Ringler, Mark Petersen, Robert L Higdon, Doug Jacobsen, Philip W Jones, and Mathew Maltrud. A multi-resolution approach to global ocean modeling. *Ocean Modelling*, 69:211–232, 2013.

[16] Xudong Yang, Xuexian Pi, Liang Zeng, and Sikun Li. Gpu-based real-time simulation and rendering of unbounded ocean surface. In *Ninth International Conference on Computer Aided Design and Computer Graphics (CAD-CG'05)*, pages 6–pp. IEEE, 2005.

[17] Hajar Righi. *Hybrid electric aircraft*. Mississippi State University, 2016.

[18] Matt Pharr, Wenzel Jakob, and Greg Humphreys. *Physically based rendering: From theory to implementation*. Morgan Kaufmann, 2016.

[19] Kyung-Duck Suh, Hyuk-Dong Kwon, and Dong-Young Lee. Some statistical characteristics of large deepwater waves around the korean peninsula. *Coastal Engineering*, 57(4):375–384, 2010.

[20] Nathan Koenig and Andrew Howard. Design and use paradigms for gazebo, an open-source multi-robot simulator. In *2004 IEEE/RSJ International Conference on Intelligent Robots and Systems (IROS)(IEEE Cat. No. 04CH37566)*, volume 3, pages 2149–2154. IEEE, 2004.

[21] Radu Horaud, Bernard Conio, Olivier Leboulleux, and Bernard Lacolle. An analytic solution for the perspective 4-point problem. *Computer Vision, Graphics, and Image Processing*, 47(1):33–44, 1989.

[22] Lijun Ding and Ardeshir Goshtasby. On the canny edge detector. *Pattern recognition*, 34(3):721–725, 2001.

[23] Nahum Kiryati, Yuval Eldar, and Alfred M Bruckstein. A probabilistic hough transform. *Pattern recognition*, 24(4):303–316, 1991.

[24] Zhiyong Ye, Yijian Pei, and Jihong Shi. An improved algorithm for harris corner detection. In *2009 2nd International Congress on Image and Signal Processing*, pages 1–4. IEEE, 2009.

[25] Brian Karis and Epic Games. Real shading in unreal engine 4. *Proc. Physically Based Shading Theory Practice*, 4(3):1, 2013.

[26] Morgan Quigley, Ken Conley, Brian Gerkey, Josh Faust, Tully Foote, Jeremy Leibs, Rob Wheeler, Andrew Y Ng, et al. Ros: an open-source robot operating system. In *ICRA workshop on open source software*, volume 3, page 5. Kobe, Japan, 2009.

[27] Hwankee Cho. A study on the configuration modeling and aerodynamic analysis of small airplanes for flight training. *Journal of the Korean Society for Aviation and Aeronautics*, 28(1):59–65, 2020.

[28] Xin Chen, Di He, and Ling Pei. Bds b1i multipath channel statistical model comparison between static and dynamic scenarios in dense urban canyon environment. *Satellite Navigation*, 1(1):1–16, 2020.

X ue Weili received a bachelor's degree in engineering and graduated from Huazhong University of Science and Technology majoring in electronic information engineering in 2020. He is currently a postgraduate student at Shanghai Jiao Tong University. His current research interests include virtual reality and autonomous driving simulation.

Z hen Sun received his B.S. degree from Harbin Institute of Technology in 2017 and M.S. degree from Shanghai Jiao Tong University in 2020, and has been pursuing his Ph.D. degree at Shanghai Jiao Tong University since then. His current research interests are in the research of theoretical methods of brain-like navigation for unknown and complex environments.

K ehui Ma received the B.Eng. degree in Intelligent Science and Technology from the school of Xidian University, China, in 2022.He is currently a Phd candidates in Shanghai Jiao Tong University. His current research interests include reinforcement learning and embodied navigation.

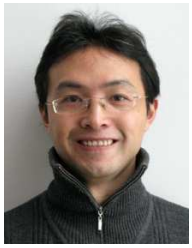

L ing Pei (Senior Member, IEEE) received the Ph.D. degree from Southeast University, Nanjing, China, in 2007. From 2007 to 2013, he was a Specialist Research Scientist with the Finnish Geospatial Research Institute. He is currently a Professor with the School of Electronic Information and Electrical Engineering, Shanghai Jiao Tong University. He has authored or co-authored over 100 scientific papers. He is also an inventor of 24 granted patents. His main research is in the areas of indoor/outdoor seamless positioning, ubiquitous computing, wireless positioning, Bio-inspired navigation, context-aware applications, location based services, and navigation of unmanned systems. Dr. Pei was a recipient of the Shanghai Pujiang Talent in 2014.

Journal of Global Positioning Systems (*2022*)
Vol. 18, No. 2: 114-122
DOI: 10.5081/jgps.18.2.114

Journal of Global Positioning Systems
2022
© CPGPS

GPS/MEMS IMU/UWB tightly coupled integrated navigation with robust Kalman filter based on bifactor[1]

Jiaxing Zhao[1,2], Jian Wang(✉)[1]

1. School of Geomatics and Urban Spatial Informatics, Beijing University of Civil Engineering and Architecture, Beijing, China
2. School of Architecture and Urban Planning, Beijing University of Civil Engineering and Architecture, Beijing, China

✉: **corresponding author,** wangjian@bucea.edu.cn

Abstract：Robust estimation has been extensively employed and developed in the integrated navigation of Global Positioning System (GPS) receivers and Micro-Electro-Mechanical System (MEMS) Inertial Measurement Unit (IMU). To further reduce or even eliminate the influence of abnormal measurements from GPS receivers/MEMS IMU, the range measurements of Ultra-Wideband (UWB) are introduced. This article proposes a GPS/MEMS IMU/UWB tightly coupled integrated navigation with robust Kalman filter based on bifactor. The proposed model consists of two main components: one is the detection of gross errors, which involves constructing an equivalent weight matrix based on bifactor weight elements; and another is estimation, from which the optimal estimation results are obtained. Finally, the simulated test and field test are carried out to verify the proposed model, and the effectively results of the new robust Kalman filter are drawn.

Keywords: Tightly coupled integrated navigation system; Bifactor weight model; Abnormal measurements; Robust estimation

1 Introduction

Global Navigation Satellite System (GNSS) receivers and Micro-Electro-Mechanical System (MEMS IMU) are commonly employed for providing position, velocity and attitude information for moving platform (Han and Wang 2017). Meanwhile, GNSS receivers have been widely used for vehicles navigating with the help of MEMS IMUs or other sensors, which can generally obtain sub-meter-level positioning accuracy in open-sky environments, it faces challenges in urban canyons, tunnels, bridges, and indoor areas where the GNSS signals will be interfered, cut off, or even unavailable (An et. al 2019; Luo and Wang 2017). High-accuracy positioning results will be obtained from GNSS can reduce or eliminate the accumulated systematic errors over time associated with MEMS IMUs (Chen et. al 2021). Ultra-Wideband (UWB) technology has been shown effective in compensating measurement errors and improving positioning performance of GNSS/MEMS IMU integrated systems (Zhang et. al 2020a, 2020b; Wang et. al 2022; Zhong et. al 2020).

Compared with the integration of GNSS and MEMS IMU, an integrated GNSS/MEMS IMU/UWB system (Chen et. al 2021; Zhang et. al 2020a; Sun et. al 2022; Li et. al 2016; Jiang et. al 2021) offers better control the influence of gross errors, and achieves a higher positioning accuracy (Li

Editor in charge: Dr. Xiaoji Niu

et. al 2018). The Kalman filter is commonly used for integrated navigation to obtain optimal estimation, under the assumption of normal distributions for measurement and state vectors. Researchers have developed various models and systems to control the divergence of positioning errors and improve the reliability of state estimation, such as fading adaptive Kalman filtering model, factor graph, adaptive filtering model and robust estimation model (Luo et. al 2017; Yang et. al 2010). Sun et al. (2022) proposed a motion model-assisted GNSS/MEMS IMU integrated navigation system on the basis of a constant yaw rate and velocity (CTRV) model, significantly improving the horizontal accuracy. Zhang et al. (2020a) designed a federal Kalman filtering model for loosely coupled GNSS/IMU/UWB integration system, which can obtain the stable and reliable results, it also can effectively resist the influence of unreliable signals. Navarro et al. (2019) constructed a low-cost GNSS/INS/UWB integration system, it can operate in standalone mode when no additional infrastructure. Jiang et al. (2021) established a tightly coupled GNSS/INS/UWB integrated navigation system, which used the UWB/INS tightly coupled integration to correct the INS accumulation errors with range information from UWB. To eliminate or weaken the influence of gross errors, Li et al. (2016) proposed a tightly coupled GNSS/IMU/UWB integrated navigation system with a robust Kalman filtering model based on Mahalanobis distance, which improved the performance of integrated navigation system. Wang et al. (2016) proposed a tightly coupled GPS/INS/UWB cooperative positioning system, in which the UWB ranging information is used to augment the GPS measurements，which can eliminate the influence of gross errors. Although Yang et al. (2002) constructed a bifactor equivalent weight model based on measurement outliers for GPS survey, its applications in integrated navigation and positioning have been limited (Chen and Shen 2020). Based on this point, to explore the performance of GPS/MEMS IMU integrated navigation, we designed a GPS/MEMS IMU/UWB tightly coupled integrated navigation system with robust Kalman filter based on bifactor. Accordingly, this article focuses on analyzing the performance and positioning accuracy of GNSS/MEMS IMU/UWB integration system.

2 GPS/MEMS IMU/UWB tightly coupled navigation system

The dynamic model of GPS/MEMS IMU/UWB tightly coupled navigation system is expressed by the following MEMS IMU error equation

$$\begin{cases} \delta\dot{\mathbf{r}} = -\omega_{en}\times\delta\mathbf{r} + \delta\mathbf{v} \\ \delta\dot{v} = -\left(2\omega_{ie}+\omega_{en}\right)\times\delta\mathbf{v} - \delta\psi\times f + \eta \\ \delta\dot{\psi} = -\left(\omega_{ie}+\omega_{en}\right)\times\delta\psi + \varepsilon \\ \dot{\eta} = u_{\eta} \\ \dot{\varepsilon} = u_{\varepsilon} \end{cases} \tag{1}$$

wherein $\delta\mathbf{r}$、$\delta\mathbf{v}$、$\delta\psi$ stand for the error vectors of position, velocity and orientation, respectively. ω_{en} is the earth rotation angular velocity vector of the geographic coordinate system relative to the coordinate system, ω_{ie} is the rotating angular velocity vector of the earth coordinate system relative to the inertial coordinate system, f is the acceleration force vector and η is the acceleration error vector, and ε is gyroscope drift error vector during the random walk process. u_{η} and u_{ε} are Gaussian white noise vectors. The generalized system model can be expressed as follows

$$\mathbf{X}_k = \mathbf{F}\mathbf{X}_{k-1} + \mathbf{u}_k \tag{2}$$

wherein $\mathbf{X}_k$ is an m×1 unknown state vector at time instant t_k, $\mathbf{F}$ is an n×m system transition matrix, $\mathbf{u}_k$ is an n×1 zero-mean Gaussian white noise vector, and the corresponding covariance matrix is $\boldsymbol{Q}$. The predicted state vector is

$$\bar{\mathbf{X}}_{\boldsymbol{k}} = \mathbf{F}\hat{\mathbf{X}}_{\boldsymbol{k}} \tag{3}$$

The measurement model of GPS/MEMS IMU/UWB integrated navigation is defined as follows

$$\mathbf{Z}_k = \mathbf{H}\mathbf{X}_k + \boldsymbol{\tau}_k \tag{4}$$

with

$$\mathbf{Z} = \begin{bmatrix} P_j^{\mathrm{GPS}} - P_j^{\mathrm{INS}} \\ D_j^{\mathrm{GPS}} - D_j^{\mathrm{INS}} \\ r_i^{\mathrm{UWB}} - r_i^{\mathrm{INS}} \\ \vdots \end{bmatrix} \tag{5}$$

wherein P_j^{GPS} and D_j^{GPS} represent the pseudorange and Doppler measurements of the j*th* GPS satellite. P_j^{INS} and D_j^{INS} stand for the predicted pseudorange and Doppler measurements of the j*th* GPS satellite by MEMS IMU, r_i^{UWB} is the UWB range measurement by two UWB units. r_i^{INS} is the derivation calculation range by MEMS IMU. $\mathbf{H}$ is an n×m measurement matrix, $\boldsymbol{\tau}_k$ is the measurement noise vector, which conforms to zero-mean Gaussian white noise with the covariance matrix $\mathbf{R}$. The residual equations of the measurement vector and the predicted state vector are

$$\mathbf{V}_k = \mathbf{H}\hat{\mathbf{X}}_k - \mathbf{Z}_k \tag{6}$$

$$\mathbf{V}_{\bar{\mathbf{X}}_k} = \hat{\mathbf{X}}_k - \bar{\mathbf{X}}_k \tag{7}$$

wherein the dimensions of $\mathbf{V}_{\bar{\mathbf{X}}_k}$ and $\mathbf{V}_k$ are m and n, respectively. $\bar{\mathbf{X}}_k$ is the predicted state vector with its covariance matrix $\boldsymbol{\Sigma}_{k/k-1}$, $\hat{\mathbf{X}}_k$ is the currently estimated state vector, and $\mathbf{Z}_k$ is an n×1 measurement vector with its covariance matrix R_k.

3 Bifactor robust estimation solution

An improved standard Kalman filter, robust Kalman filter based on bifactor, has been developed using the weight matrix of the measured and estimated information. The Least-Squares cost function at the observation epoch *k* is given as follows (Wang et. al 2021)

$$\boldsymbol{\Omega} = \mathbf{V}_k^T \mathbf{R}_k^{-1} \mathbf{V}_k + \mathbf{V}_{\bar{\mathbf{X}}_k}^T \boldsymbol{\Sigma}_{k/k-1}^{-1} \mathbf{V}_{\bar{\mathbf{X}}_k} = \mathbf{min} \tag{8}$$

wherein $\bar{\mathbf{P}}$ is called an equivalent weight matrix, $\bar{p}_{ij}$ is an element of the bifactor equivalent weight matrix, γ_{ii} and γ_{jj} are the factors of adaptive equivalent weight elements.

$$\bar{p}_{ij} = p_{ij}\gamma_{ij} \tag{9}$$

$$\gamma_{ij} = \sqrt{\gamma_{ii}\gamma_{jj}} \tag{10}$$

The robust Kalman filtering model based on bifactor consists of adaptive factor construction and iteration solutions. The IGG III model is introduced, and the adaptive factors γ_{ii} could be chosen as follows

$$\gamma_{ii} = \begin{cases} 1 & |\tilde{v}_i| \le k_0 \\ \dfrac{k_0}{|\tilde{v}_i|}\dfrac{k_1 - |\tilde{v}_i|}{k_1 - k_0} & k_0 < |\tilde{v}_i| \le k_1 \\ 0 & |\tilde{v}_i| > k_1 \end{cases} \tag{11}$$

wherein γ_{jj} is the same as γ_{ii}, $\tilde{v}_i$ is a standardized residual vector element for detection the presences of gross errors, when $|\tilde{v}_i| \le k_0$, the gross errors exist. k_1 and k_0 are two constants, usually chosen as $1.0 \sim 1.5$ and $2.5 \sim 8.0$. Then, we obtain the new robust estimation is obtained as follows

$$\hat{\mathbf{X}}_k = (\mathbf{A}^T\mathbf{P}\mathbf{A})^{-1}\mathbf{A}^T\mathbf{P}\mathbf{L}_k \tag{12}$$

wherein $\mathbf{A} = \begin{bmatrix} \mathbf{H} \\ \mathbf{I}_{\mathrm{m}} \end{bmatrix}$, $\mathbf{L}_k = \begin{bmatrix} \mathbf{Z}_k^T & \bar{\mathbf{X}}_k^T \end{bmatrix}$ and $\mathbf{P} = \begin{bmatrix} \mathbf{R}_k & \\ & \boldsymbol{\Sigma}_{k/k-1} \end{bmatrix}$, the matrix $\mathbf{I}_{\mathbf{m}\times\mathbf{m}}$ stands for a m×m unit matrix. The corresponding covariance matrix of the estimated state vector is

$$\boldsymbol{\Sigma}_{\hat{X}} = \hat{\sigma}_0^2(\mathbf{A}^T\mathbf{P}\mathbf{A})^{-1} \tag{13}$$

wherein $\hat{\sigma}_0^2 = \dfrac{\mathbf{V}_k^T \mathbf{R}_k^{-1}\mathbf{V}_k + \mathbf{V}_{\bar{\mathbf{X}}_k}^T \boldsymbol{\Sigma}_{k/k-1}^{-1}\mathbf{V}_{\bar{\mathbf{X}}_k}}{n}$ is the posteriori variance of unit weight (Wang 2008, 2009).

4 Experiments

To verify the effectiveness of the proposed technique, simulation and field tests were conducted. The field test was carried out on the roof of the Nottingham Geospatial Institute (NGI).

4.1 The simulated test

The simulated test was designed to evaluate the performance of the proposed model. A vehicle is

traveling along a road, and the movement model of the vehicle can be written as

$$\boldsymbol{x}_{k+1} = \begin{bmatrix} 1 & 0 & \mathbf{T} & 0 \\ 0 & 1 & 0 & \mathbf{T} \\ 0 & 0 & 1 & 0 \\ 0 & 0 & 0 & 1 \end{bmatrix} \boldsymbol{x}_k + \boldsymbol{w}_k \qquad (14)$$

$$\boldsymbol{z}_k = \begin{bmatrix} 1 & 0 & 0 & 0 \\ 0 & 1 & 0 & 0 \end{bmatrix} \boldsymbol{x}_k + \boldsymbol{\tau}_k \qquad (15)$$

wherein k represents the epoch time, the 2000 epochs of data were utilized to verify the proposed model, $x_k = [p_N \quad p_E \quad v_N \quad v_E]^T$, p_N and p_E represent the position of the vehicle in the North and East directions, v_N and v_E represent the velocity in the North and East directions, $\mathbf{T}$ represents the sampling step size, w_k represents the process noise, and v_k represents the measurement noise. w_k and v_k obey Gaussian distributions, and y_k represents the measurement position of vehicle. The covariance matrix of the process noise is $\mathbf{Q} = diag(4,4,1,1)$, the covariance matrix of the measurement noise is $\mathbf{R} = diag(900,900)$, the initial estimation error covariance matrix is $P_0 = diag(4,4,1,1)$, and the initial state of the vehicle is $x_0 = [1 \quad 1 \quad 0 \quad 0]^T$.

Table 1 RMSE of standard Kalman filter and robust Kalman filter (the simulated test)

	North (m)	East (m)
Standard Kalman filter	43.86	60.12
Robust Kalman filter (bifactor)	13.11	13.07

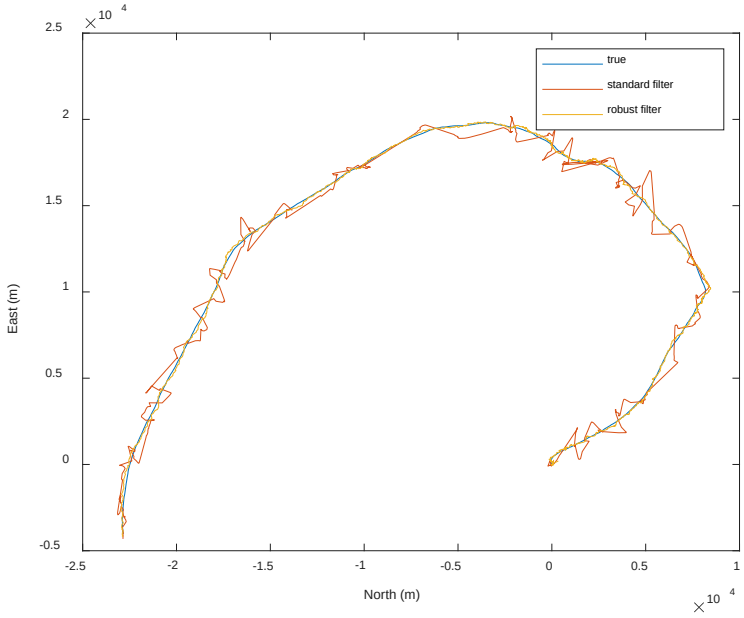

Figure 1 Trajectory of vehicle (true, standard and robust filters)

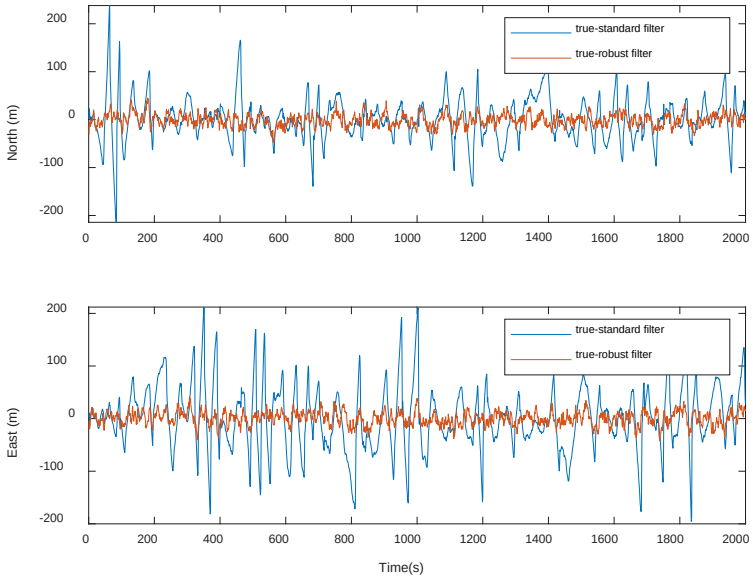

Figure 2 Position error of the vehicle in the North and East directions

Figure 1 shows a simulated test. The position error of a vehicle in the North and East directions are given in Figure 2. In comparison with standard Kalman filter, the robust Kalman filtering model based on bifactor results in a better positioning performance. The Root Mean Squared Error (RMSE) of standard Kalman filter and robust Kalman filter is given in Table 1, which clearly demonstrates that the proposed model significantly improved positioning accuracy in the North and East directions by 70% and 78%.

4.2 Field test

The performance of the proposed model has been evaluated via a field test, and we constructed a GPS/MEMS IMU/UWB tightly coupled integrated navigation with robust Kalman filter based on bifactor. The test consists of one MEMS IMU measurement unit, three UWB measurement units, and two GNSS receivers. One GNSS receiver is mounted on the carrier vehicle, while one UWB unit was fastened under the antenna with a known lever-arm, another GNSS receiver was set on the roof to act as the reference station, and other two UWB units were mounted on pillars on the roof of NGI, known coordinates, the r_1^{UWB} and r_2^{UWB} ranges were obtained. The duration of the field test is 815 seconds. The number of the tracked satellites was from 6 to 10, with an average is 9 satellites, which meets the basic positioning requirements. Figure 3 illustrates the number of satellites tracked by the GNSS receiver. The detailed description is given in (Wang et.al 2016; Li et.al 2016).

Table 2 RMSE form standard Kalman filter and robust Kalman filter (the field test)

	North (m)	East (m)	Down (m)
Standard Kalman filter	3.29	1.27	1.52
Robust Kalman filter (bifactor)	1.06	0.46	1.29

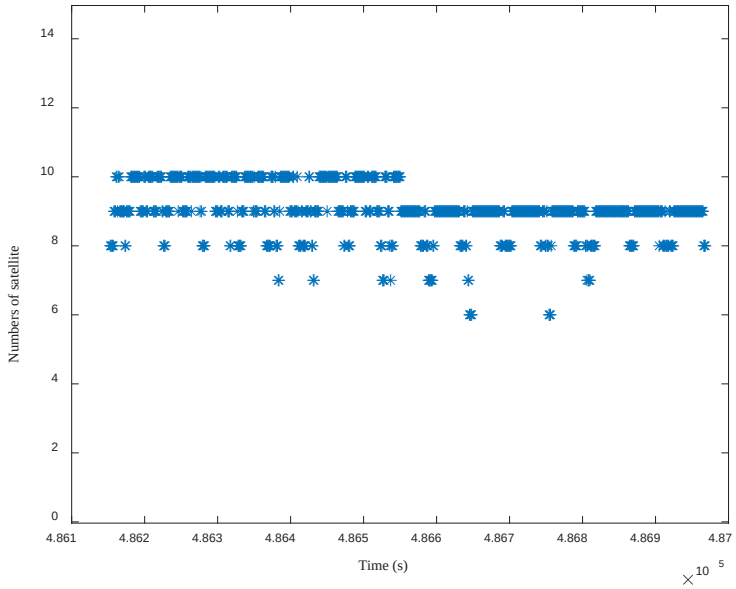

Figure 3 Number of satellites tracked by GPS receiver

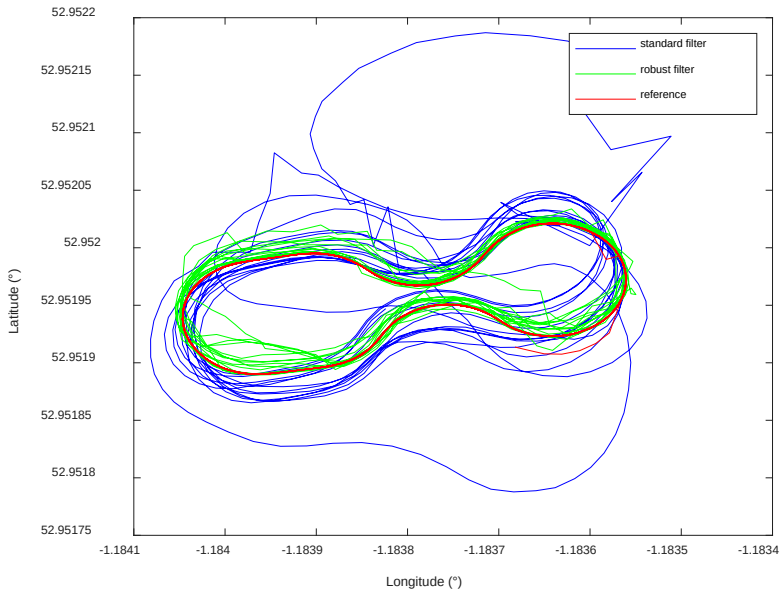

Figure 4 Filed trajectory of carrier vehicle

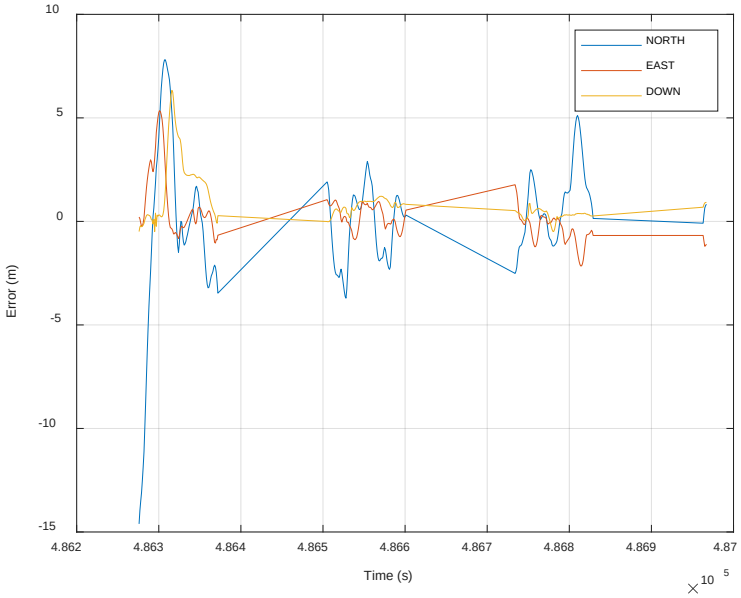

Figure 5 Position error of standard Kalman filter

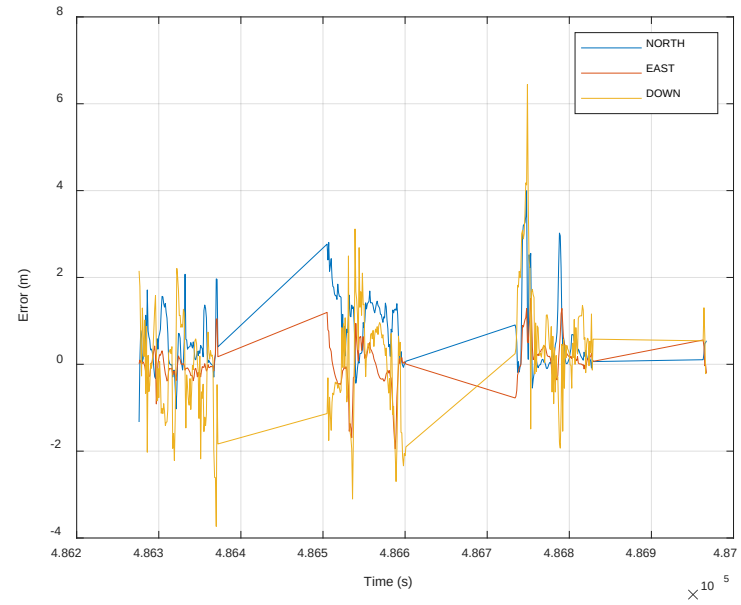

Figure 6 Position error of robust Kalman filter based on bifactor

The simulated test verifies the effectiveness of the robust Kalman filtering model based on bifactor, and the filed test of GPS/MEMS IMU/UWB was conducted to evaluate the performance of proposed model. Figure 4 shows the field test of carrier vehicle in the NGI, with the reference trajectory represented by the red line, the trajectory estimated using the standard Kalman filter represented by the blue line, and the green line trajectory corresponds to the trajectory obtained using the robust Kalman filtering model based on bifactor. Figures 5 and 6 demonstrate the position error of two models in North, East and Down directions. RMSE of different filtering models is shown in Table 2，it clearly presents that the proposed model improved positioning accuracy in the North，East and Down directions by 68%, 64%, and 15%, respectively.

5 Conclusion

In this article, we proposed a robust Kalman filtering model based on bifactor for a GPS/MEMS IMU/UWB tightly coupled integrated navigation system. Through the simulated and field tests, the better positioning results were obtained with the proposed model especially in the presence of gross errors in the measurement processing. The proposed model effectively reduced the influence of the outlying measurements. However, it should be noted that this article focused on constructing a tightly coupled integrated navigation system and did not consider various scenarios such as sheltered environments and semi-sheltered environments, which will be addressed in future research endeavors.

Acknowledgment:

The authors acknowledge the Beijing Natural Science Foundation of China for its financial support (No. 8222011), and BUCEA Doctor Graduate Scientific Research Ability Improvement Project: DG2023006.

Reference

An J, Lee J (2019): Robust positioning and navigation of a mobile robot in an urban environment using a motion estimator, Robotica, 37(8), 1320-1331.

Chen H, Chang L, Xu Z, Ye W, Wu C (2021): UAV collaborative navigation algorithm based on tight combination of GNSS / INS /UWB in complex environment, Chinese Journal of Scientific Instrument, 42(07), 98-107.

Chen J, Shen Y (2020): An Improved Robust Estimation Algorithm for Correlated Observations, Journal of Geodesy and Geodynamics, 40(05): 507-511.

Han H, Wang J (2017): Robust GPS/BDS/INS tightly coupled integration with atmospheric constraints for long-range kinematic positioning, GPS Solutions, 21, 1285-1299.

Jiang W, Cao Z, Cai B, Li B, Wang J (2021): Indoor and outdoor seamless positioning method using UWB enhanced multi-sensor tightly-coupled integration. IEEE Transactions on Vehicular Technology, 70(10), 10633-10645.

Li Z, Chang G, Gao J, Wang J, Hernandez A (2016): GPS/UWB/MEMS-IMU tightly coupled navigation with improved robust Kalman filter, Advances in Space Research, 58(11), 2424-2434.

Navarro M, Arribas J, Vilà-Valls J, Casademont J, Calveras A, Catalán M (2019): Hybrid GNSS/INS/UWB Positioning for Live Demonstration Assisted Driving, 2019 IEEE Intelligent Transportation Systems Conference (ITSC), 3294-3301.

Sun Y, Li Z, Yang Z, Shao K, Chen W (2022): Motion model-assisted GNSS/MEMS IMU integrated navigation system for land vehicle, GPS Solutions, 26(4), 131

Wang C, Xu A, Sui X, Hao Y, Shi Z, Chen Z (2022): A Seamless Navigation System and Applications for Autonomous Vehicles Using a Tightly Coupled GNSS/UWB/INS/Map Integration Scheme, Remote Sens, 14, 27.

Wang J (2008) Test Statistics in Kalman Filtering, Journal of Global Positioning Systems, 7(1):81-90.

Wang J (2009) Reliability Analysis in Kalman Filtering, Journal of Global Positioning Systems, 8(1), 101-111.

Wang J, Boda A, Hu B (2021): Comprehensive error analysis beyond system innovations in Kalman filtering – ScienceDirect, Learning Control, 59-92.

Wang J, Gao Y, Li Z, Meng X, Hancock C (2016): A tightly-coupled GPS/INS/UWB cooperative positioning sensors system supported by V2I communication, Sensors,16(7), 944.

Yang Y, Gao W, Zhang X (2010): Robust Kalman filtering with constraints: a case study for

integrated navigation, Journal of geodesy, 84, 373-381.

Yang Y, Song L, Xu T (2002): Robust estimator for correlated observations based on bifactor equivalent weights, Journal of Geodesy, 76, 353-358.

Zhang R, Shen F, Liang Y, Zhao D (2020a): Using UWB Aided GNSS/INS Integrated Navigation to Bridge GNSS Outages Based on Optimal Anchor Distribution Strategy, 2020 IEEE/ION Position, Location and Navigation Symposium (PLANS), 1405-1411.

Zhang R, Shen F, Li Q (2020b): A Hybrid Indoor/Outdoor Positioning and Orientation Solution Based on INS, UWB and Dual-Antenna RTK-GNSS, 2020 27th Saint Petersburg International Conference on Integrated Navigation Systems (ICINS), 1-5.

Zhong L, Wang R, Wang Y, Ni Y, Liu X, Wang L (2020): Optimizing INS/GNSS/UWB integrated vehicle collaboration navigation based on performance analysis under crowded environments, 2020 3rd International Conference on Unmanned Systems (ICUS), 1042-1046.

Authors

Jiaxing Zhao is currently a Ph.D. candidate at the School of Geomatics and Urban Spatial Informatics, Beijing University of Civil Engineering and Architecture, China. He obtained his M.Sc. degree from Anhui University of Science and Technology in 2021. His current research interests include multi-sensor data fusion for positioning and navigation.

Jian Wang is a professor at Beijing University of Civil Engineering and Architecture, China. He obtained his Ph.D. degree in 2006 from China University of Mining and Technology, China. His current research interests include precise GNSS positioning, GPS/INS and other sensors integrated navigation.

Journal of Global Positioning Systems (*2022*)
Vol. 18, No. 2: 123-133
DOI: 10.5081/jgps.18.2.123

Two-stage fusion localization based on UWB/PDR/Geomagnetism in underground space

Jinkun Li[1], Chundi Xiu[1 *], Dongkai Yang[1], Maria S. Selezneva[2]

1. School of Electronic and Information Engineering, BeiHang University, jkl_Reuben@163.com, edkyang@buaa.edu.cn;
2. Department of Automatic Control Systems, Bauman Moscow State Technical University, m.s.selezneva@mail.ru

* Corresponding author,

Abstract: A two-stage fusion positioning model based on UWB/PDR/Geomagnetism is proposed for pedestrian positioning in underground space. Firstly, an improved particle filter (PF) based on regional constraint is applied to PDR/Geomagnetism combination positioning, where the PDR positioning results are used to constrain the geomagnetic matching region. The proposed algorithm improves the inherent blindness of scattered particles of traditional PF, thus to enhance the positioning accuracy. Furtherly, Factor graph (FG) is used to fuse the output of PF above with the UWB positioning results, which effectively overcomes the serious problem of positioning hopping points caused by signal occlusion in some areas of UWB system. Experimental results show that the improved PF can outperform extended Kalman filter (EKF) for PDR/Geomagnetism combination positioning and FG algorithm can provide a higher positioning accuracy for UWB/PDR/Geomagnetism fusion positioning.

Keywords: Underground space; Pedestrian Dead Reckoning; Geomagnetic matching positioning; Ultra WideBand; Particle filter; Factor graph

I. Introduction

With the rapid development of society and technology, utilization of underground space is getting more and more extensive, from shallow utilization to large-scale development, from solving urban problems to enhancing urban competitiveness, the intensive and composite utilization of underground space resources has been regarded as a standard paradigm to support the sustainable development of urban modernization. The challenge of pedestrian localization in underground space is mainly reflected in its closed characteristics, which is a typical radio denial environment. And the existing GNSS, WiFi, 4G and other wireless networks cannot be valid. Due to the increasing demand for location-based services, research on effective pedestrian localization in underground space becomes a hot topic due to the increasing demand for Location Based Service (LBS) [1-2].

At present, indoor positioning technology for underground space has been in-depth research by scholars, and indoor positioning technology based on geomagnetism, visible light, inertial guidance and UWB has been widely used and developed[3-6]. Among many technologies, UWB has recently become effective solution to high positioning accuracy and strong anti-interference. However, it also has its own shortcomings, which is the serious attenuation of positioning accuracy in areas where the signal is occluded. Based on this, it is considered to integrate PDR and geomagnetism, two positioning

Editor-In-Charge: Dr. Wu Chen

technologies that do not require additional infrastructure.

Many studies have been carried out on PDR and geomagnetism, as well as UWB and PDR combined localization methods. As reported briefly in [7], an IMU localization algorithm based on magnetic constraints uses multi-stage Fourier transform method to extract features, whose average error of the trajectory under loop closure constraint is controlled below 2.15 m. Song Biao et al. [8] designed an inertial guidance-assisted geomagnetic indoor positioning system for mobile phones, which achieved good positioning accuracy in two-dimensions, but could not adapt well to three-dimensional complex environment. Reference [9] aiming at the shortcomings of low recognition of geomagnetic signals and the problem of error accumulation of PDR, the particle filter algorithm is used to fuse the geomagnetism and PDR positioning results, whose positioning error can reach more than 80% within 1.5m. An improved particle filtering method is proposed in [10]. Comparing with the traditional particle filter, multi-dimensional dynamic time warping (MD-DTW) is used to constrain the length of the particle sequence and the method of segmented particle weighting, which can effectively accelerate the convergence speed of particle filtering. As reported briefly in [11], the methods of dead-assisted UWB positioning and UWB-assisted dead reckoning are adopted, which enhances the advantages of UWB positioning, and the maximal positioning error is within 2m. Zhu Caijie[12] proposed an algorithm using INS to assist UWB positioning, which can effectively make up for the shortcomings of UWB positioning technology in the positioning process. And in terms of the mean positioning error, the algorithm based on Kalman filter (KF) can improve 0.1m in x-axis and 0.2m in y-axis. Benzerrouk put forwards to use cubature Kalman filter (CKF) as a superior alternative to standard filters which improves the mean and covariance propagation consequently[13]. However, the above methods mainly depend on filter fusion methods, and when the information of one sensor fails or becomes unavailable, Kalman filter and other complex system are required to be reconstructed to deal with the problems, resulting in disadvantages such as high cost-effectiveness ratio and large memory consumption. For wireless communication positioning methods, the visibility of the signal is one of the factors that affect the positioning accuracy. Under the influence of non-line-of-sight (NLOS) [14], there are some hopping points in all positioning reference points. Reference [15] describes one base station (BS) based distance and angle positioning algorithm with extended Kalman filter (DAPA-EKF) in NLOS environment, which significantly outperforms the reference methods under various NLOS situations. Mingxiang Liao et al. [16] presents a Chan-Taylor-Kalman (CTK) joint positioning algorithm based on UWB and adapted to NLOS environment, which indicates that the probability of the positioning error of the CTK joint positioning algorithm greater than l0cm is only about 10%.

To make full use of various indoor positioning methods, some scholars propose to construct a data fusion algorithm framework with dynamic topology based on the relevant theory of FG [17-18]. The fusion algorithm framework based on the factor graph model can effectively solve the problem of a sensor failure in data fusion, and has good scalability for multiple sensors. Therefore, it can flexibly configure sensors[19-20]. Factor graph is a kind of probability graph model, first used in the field of coding[21-22], has gradually been applied to artificial intelligence, positioning navigation and other fields in recent years. One of the applications in the field of navigation is information fusion positioning system. Moreover, factor graph can realize the plug and play of system sensors and has been widely concerned in the field of combined navigation.

In this paper, a two-stage fusion localization model based on UWB/PDR/geomagnetism is proposed. This paper is organized as follows. In section Ⅱ, it introduces the concret detail about two-stage fusion localization model. Improved PF combination positioning method based on PDR/geomagnetism and FG fusion positioning method base on UWB/PDR/geomagnetism are included. Section Ⅲ conducts numerical

experiments to evaluate positioning performance of the proposed algorithm. And conclusions are given in last section.

II. Two-Stage Fusion Localization Model and Algorithm

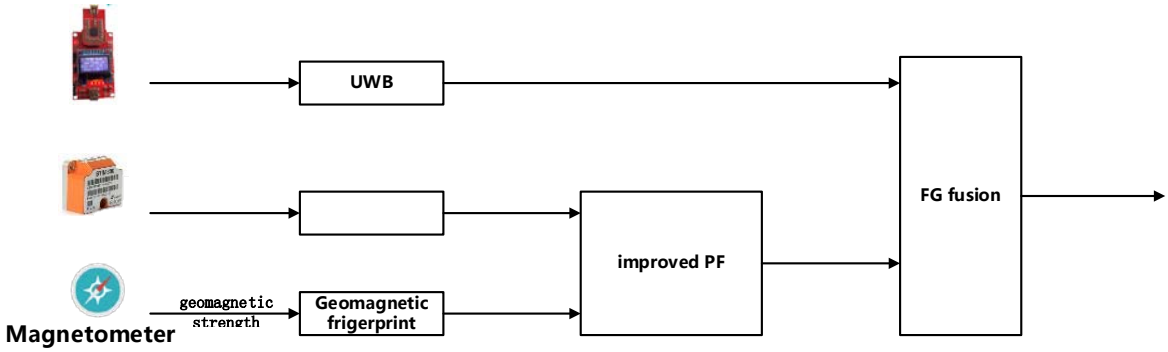

Fig.1 Two-stage fusion localization model

Two-stage fusion localization model is shown in Fig.1. The improved PF algorithm using regional constraints combines the PDR and geomagnetism localization. FG is employed for UWB/PDR/geomagnetism multi-source fusion positioning, which effectively improves the continuity and stability of pedestrian positioning in underground space.

Improved PF Fusion Algorithm for PDR/Geomagnetism Combination

In the first stage of localization, the positioning error of PDR accumulates seriously over time. Geomagnetism positioning employs fingerprint matching method, which has big positioning error because of low fingerprint resolution within a large area. In order to decrease the mismatching rate, the improved PF is used for PDR/geomagnetism combination. PDR positioning result is employed to constrain the fingerprint database area while geomagnetism positioning result corrects PDR positioning result. The PF employs a group of particles to approximate a posterior probability distribution effectively estimating nonlinear non-Gaussian systems. Let the equations of state and observations for nonlinear systems be:

$$\mathbf{x}_k = f_k\left(\mathbf{x}_{k-1}, \boldsymbol{\omega}_{k-1}\right) \quad (1)$$

$$\mathbf{z}_k = h_k\left(\mathbf{x}_k, \mathbf{v}_k\right) \quad (2)$$

In (1) and (2), X_k is the system states, ω_k is the process noise and V_k is the observed noise.

The state prediction equation can be expressed as:

$$p\left(\mathbf{x}_k \mid \mathbf{z}_{1:k-1}\right) = \int p\left(\mathbf{x}_k \mid \mathbf{x}_{k-1}\right) p\left(\mathbf{x}_{k-1} \mid \mathbf{z}_{1:k-1}\right) d\mathbf{x}_{k-1} \quad (3)$$

The state update equation is:

$$p\left(\mathbf{x}_k \mid \mathbf{z}_{1:k}\right) = \frac{p\left(\mathbf{z}_k \mid \mathbf{x}_k\right) p\left(\mathbf{x}_k \mid \mathbf{z}_{1:k-1}\right)}{\int p\left(\mathbf{z}_k \mid \mathbf{x}_k\right) p\left(\mathbf{x}_k \mid \mathbf{z}_{1:k-1}\right) d\mathbf{x}_k} \quad (4)$$

The essence of PF is to use the sum of finite sample points instead of integral operations, that is, the posterior probability density distribution of the target state at k is shown in (5).

$$p\left(\mathbf{x}_{0:k} \mid \mathbf{z}_{1:k}\right) \approx \sum_{i=1}^{N} w_k^i \delta\left(\mathbf{x}_{0:k} - \mathbf{x}_{0:k}^i\right) \quad (5)$$

Assuming that $\left\{\mathbf{x}_{0:k}^i\right\}_{i=1}^{N_s}$ is the set of particles, N_s is the total number of particles, which can be obtained from the important density function $q\left(\mathbf{x}_{0:k} \mid \mathbf{z}_{1:k}\right)$, then the particle weights can be expressed as:

$$w_k^i \propto \frac{p\left(\mathbf{x}_{0:k}^i \mid \mathbf{z}_{1:k}\right)}{q\left(\mathbf{x}_{0:k}^i \mid \mathbf{z}_{1:k}\right)} \quad (6)$$

In (6), w_k^i is the weight of the i-th particle at k, and $x_{0:k}$ is the set of states of the system from 0 to k. Sequential importance sampling is the basis for PF implementation, so Samples are drawn from the importance density function which is set to an

easily achievable prior probability. Resampling is to solve the degradation phenomenon in the process of particle transfer, which refers to the imbalance of weight distribution due to the increasing variance of weight. When the filter is seriously degraded, a large number of computing resources are wasted on particles with small weights, which affects the performance of the filter. During the resampling process, particles with large weights produce more particles while particles with small weights produce fewer particles or even discard them directly. However, this will lose the diversity of particles and affect the performance of particle filtering.

In this paper, improved PF based on regional constrain for PDR/geomagnetism is proposed. The PDR positioning result and geomagnetic strength of fingerprint database are taken as the state quantity and the real-time geomagnetic strength is taken as the observation. In the process of initializing the particles, the particles are scattered in the circle determined by the PDR positioning result as the center of the circle and the mean positioning error empirical value as the radius. A schematic diagram of regional constrain positioning is shown in Fig.2.

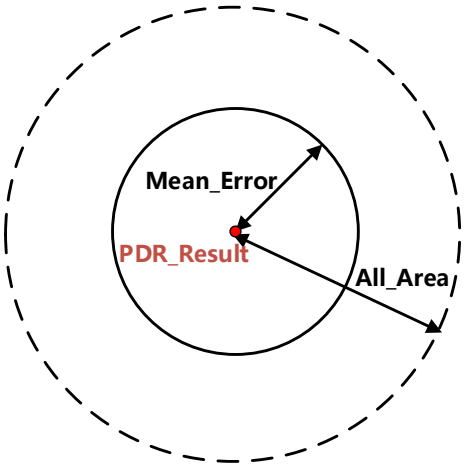

Fig.2 constrained area diagram

In the figure, the dotted circular area is the geomagnetic matching full area, and the solid circular area is the constrained geomagnetic matching area.

The improved particle filter algorithm simplifies the prediction step in traditional PF, improves the inherent blindness of particle seeding, and reduces the number of matching points with the geomagnetic fingerprint database, thus to increase the algorithm efficiency and decrease mismatching rate.

FG Fusion Algorithm for UWB/PDR/ Geomagnetic Fusion

In the second stage of localization, UWB positioning has some hopping points because of NLOS environment. FG is employed for UWB/PDR/geomagnetism fusion positioning. FG is a two-way graph based on factoring a global function with multiple variables to obtain the product of several local functions. Its basic structure, shown in Fig.3, consists mainly of variable nodes (represented by diamonds) and function nodes (represented by circles).

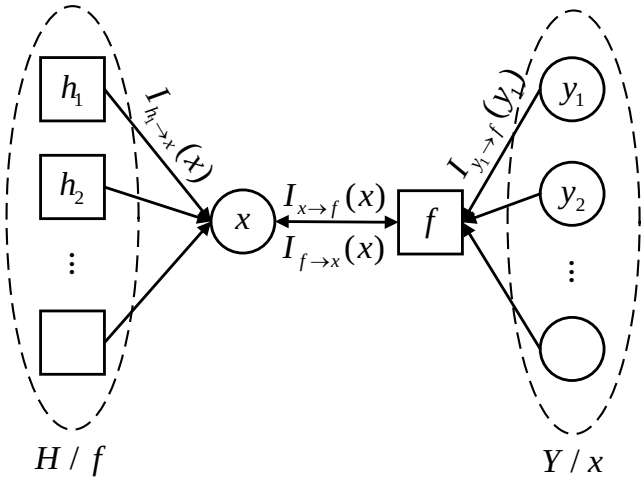

Fig.3 the sum-product algorithm

Sum product algorithm (SPA) is commonly employed to delivery message in factor graphs. Obeying the following guidelines, variable nodes to function nodes messaging:

$$\mu_{x\to f}(x)=\prod_{H/f} I_{h\to x}(x) \tag{7}$$

Messaging from function nodes to variable nodes:

$$\mu_{f\to x}(x)=\sum_{\sim x}\{f(Y)\prod_{Y/x}\mu_{y\to f}(y)\} \tag{8}$$

Where H represents the set of all function nodes connected to the variable node x union; similarly, Y represents neighbors connected to the f set of function nodes; H/f represents a neighborhood set connected to variable node x, but not included in function node f; similarly, Y/x

means that it is connected to the function node f neighborhood set, not the variable node x.

For the problem to be solved in the paper, we construct a model as follows. At time k, the state of the location target is expressed as

$$F(k) = (x_k, y_k, z_k) \tag{9}$$

where x_k, y_k, z_k indicates positioning result. Taking discrete time model, we can get the following results.

$$x_k = x_{k-1} + w_{x_k} \tag{10}$$

$$y_k = y_{k-1} + w_{y_k} \tag{11}$$

$$z_k = z_{k-1} + w_{z_k} \tag{12}$$

where w_{x_k}, w_{y_k}, w_{z_k} stand for measurement noise of position.

The initial state of location target is defined as

$$F(0) = (x_0, y_0, z_0) \tag{13}$$

According to the problem formulation, A factor graph structure model is designed as shown in Fig.4. We select different kinds of location sources which includes PDR/geomagnetic and UWB single-mode positioning result to participate in fusion process. F_{k-1} and F_k respectively represent the state of positioning target in time $k-1$ and k.

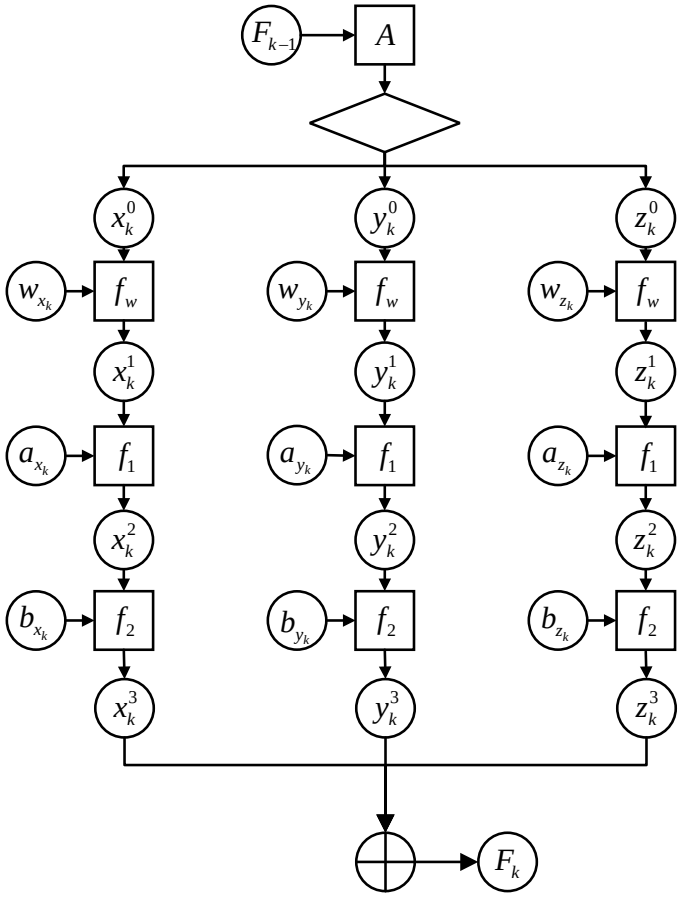

Fig.4 factor graph structure model diagram.

Since the model adopts three-dimensional coordinates, we divide the motion state into three parts: x, y, z, taking the x direction as an example, x_k^1, x_k^2,..., x_k^n is the x-coordinate value of different fusion steps at k time, and W_{x_k} is the measurement noise. a_{x_k}, b_{x_k} are PDR/geomagnetic and UWB single-mode positioning result. f_w represents a fusion function node. Fuse different variable nodes in function nodes. After a series of

soft information calculations, the fusion result x_k^n is obtained. y_k^n and z_k^n can be implemented in the same way. The fusion results x_k^n, y_k^n, and z_k^n were combined to obtain F_k.

During the fusion process, assuming that the soft message passed in the factor graph obeys Gaussian distribution with mean being m and variance being σ. We define the soft-information as

$$I = \{m_I, \sigma_I\} \tag{14}$$

Noting that the product of any Gaussian Probability Distribution Functions (PDF) is still a Gaussian PDF, so we have the following formula

$$\prod_{i=1}^{n} N = (x, m_i, \sigma_i^2) \propto N(x, m_\Omega, \sigma_\Omega^2) \tag{15}$$

where

$$\frac{1}{\sigma_\Omega^2} = \sum_{i=1}^{N} \frac{1}{\sigma_i^2} \tag{16}$$

$$m_\Omega = \sigma_\Omega^2 \sum_{i=1}^{n} \frac{m_i}{\sigma_i^2} \tag{17}$$

Here is some initialization information. the initial value of soft-information is $I_{x_k^0} = \{m_{x_k^0}, \sigma_{x_k^0}^2\}$ with initial mean x_0 and initial variance σ_0^2. $I_{w_k} = \{m_{w_k}, \sigma_{x_k^0}^2\}$ indicates the indeterminacy of the model.

In Fig.3, according to the sum-product algorithm, we can achieve the soft-information as followed

$$I_{x_k^1} = \{m_{x_k^0} + m_{w_{x_k}}, \sigma_{x_k^0}^2 + \sigma_{w_{x_k}}^2\} \tag{18}$$

Through a series of soft message solution, the n-th variable is obtained. The soft message at the node is

$$I_{x_k^n} = \{\frac{1}{1/\sigma_{x_k^{n-1}}^2 + 1/\sigma_{a_{x_k^{n-1}}}^2 + \ldots}(\frac{m_{x_k^{n-1}}}{\sigma_{x_k^{n-1}}^2} + \frac{m_{a_{x_k^{n-1}}}}{\sigma_{a_{x_k^{n-1}}}^2} + \ldots), \frac{1}{1/\sigma_{x_k^{n-1}}^2 + 1/\sigma_{a_{x_k^{n-1}}}^2 + \ldots}\} \tag{19}$$

wherein $m_{x_k^n}$ is the final fusion result in x-coordinate shown as m_x.

$$m_x = \frac{1}{1/\sigma_{x_k^{n-1}}^2 + 1/\sigma_{a_{x_k^{n-1}}}^2 + \ldots}(\frac{m_{x_k^{n-1}}}{\sigma_{x_k^{n-1}}^2} + \frac{m_{a_{x_k^{n-1}}}}{\sigma_{a_{x_k^{n-1}}}^2} + \ldots) \tag{20}$$

Consistently, m_y and m_z can be obtained in the same way. At this point, we get the state of the k moment. In the same way, we can get the state at $k+1$, $k+2$, and so on until we get the final fusion result.

III. Experimental Result

In order to verify the effectiveness of the proposed algorithm, experiments are conducted in actual underground space environment using real data. The data acquisition equipment is one-tag integrated UWB DWM1000 module and IMU module and four-base stations also containing DWM1000 module. The block photograph of BS signal is as follow in the Fig.5.

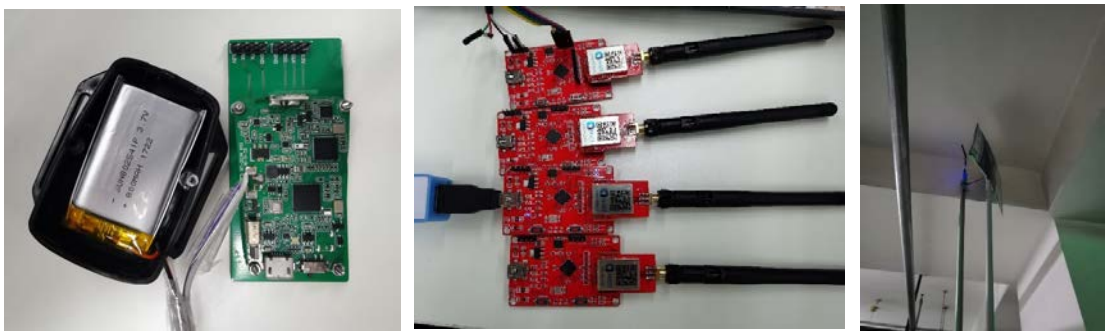

Fig.5 data Collection Equipment

Two typical experimental scenarios are selected for data collection. As shown in Fig.6, Ex 1# and Ex 2# are carried out at underground garage whose height is more than 3m, the new main building of Beihang University on the B2 floor of Block C and B1 floor of Block F respectively. The area of 15m*15m is evenly divided into grids at intervals of 1m, geomagnetic strength is collected at each mesh vertex. Table.1 shows more parameter configurations. In Ex 1# and Ex 2#, BS1(0,7,0) was blocked by paperboard as shown in Fig.5.

Table.1 parameter configuration

parameter	**configuration**
UWB positioning method	TDOA
Geomagnetie matching method	K-NearestNeighbor (K-NN)
UWB BSs coordinates	BS1(0,7,0), BS2 (4,0,3), BS3 (15,7,0), BS4 (8,15,3)
the origin of coordinates	the bottom left vertex in grid graph

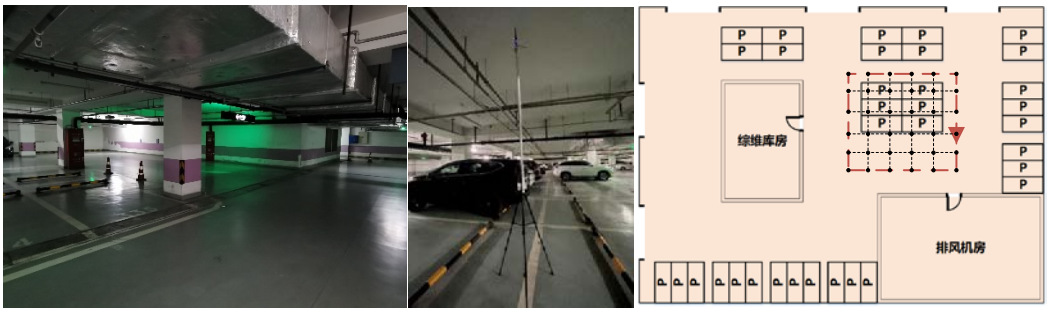

(a) scenario 1# (b) scenario 2# (c) experimental route

Fig.6 experimental scenarios

For the positioning performance estimation consideration, the mean value, standard deviation of error (STD) and cumulative distribution function (CDF) of positioning error are introduced. Table.2 shows the performance comparison of the positioning accuracy of different positioning methods and the corresponding CDF curves are shown in Fig.7

Table.2 comparison the accuracy of different positioning methods

Positioning method	mean value/m		STD/m		mean error<2m/%	
	Ex 1#	Ex 2#	Ex 1#	Ex 2#	Ex 1#	Ex 2#
PDR	2.27	2.35	1.46	1.57	53%	33%
geomagnetic	6.94	6.97	2.21	2.58	4%	5%
PF combination	1.80	1.87	1.13	0.96	69%	62%
EKF combination	2.12	2.19	1.32	1.05	56%	57%
UWB	1.64	1.74	1.03	0.99	73%	58%
Factor graph fusion	1.52	1.66	0.98	0.84	79%	71%

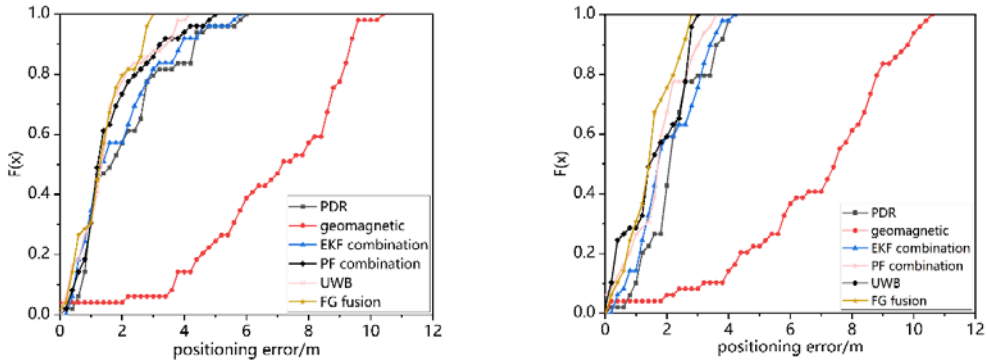

Ex 1# (b) Ex 2#

Fig.7 CDF curves of different method positioning error

For the first stage, the improved PF algorithm outperform EKF[23-24] for PDR/geomagnetism combination from Table.2 and Fig.7. In terms of mean positioning error, the positioning error of improved PF are 1.80m and 1.87m in Ex 1# and Ex 2#, which is lower than that of EKF; in terms of STD of positioning error, PF method is the lowest in all PDR and geomagnetism positioning methods, which indicates its positioning points error has less polarized; in terms of CDF of positioning error, the positioning points within 2m after PF fusion account for 69% and 62% of all reference points, which is reduced by 13% and 5% comparing with EKF. From the trajectory of Ex 1# (a) and Ex 2# (a), it's obvious that PDR accumulate seriously over time and geomagnetism has bigger error. Improved PF is closer to the real trajectory. In fact, the improved PF combine the characteristics of the fingerprint of geomagnetism and particles in traditional PF. It narrows the particle dispersal range in prediction step compared the traditional particle filter algorithm dramatically; in addition, compared with the fingerprint matching of the entire regional fingerprint database in the entire target area to be located, the improved algorithm reduces the number of matching points with the static geomagnetic fingerprint database, which improves the efficiency of the algorithm compared with the traditional PF.

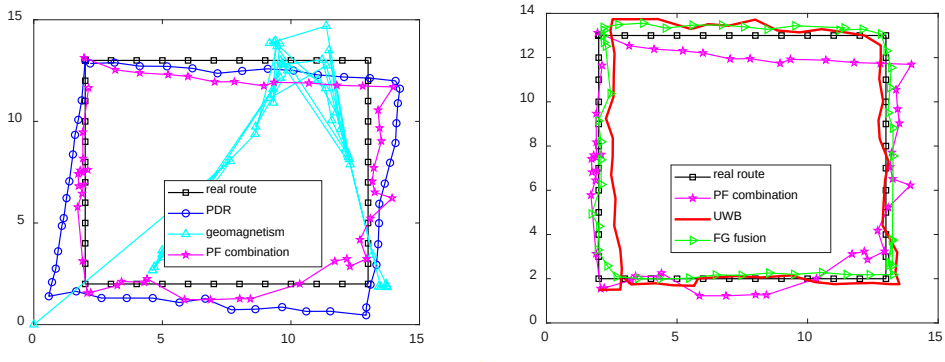

(a) PDR vs geomagnetism, PF (b) FG vs PF, UWB

Fig.8 trajectory diagram

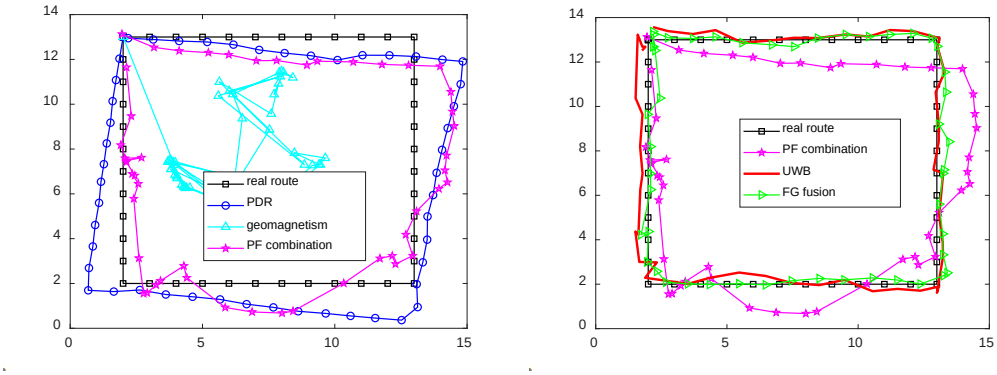

(a) PDR vs geomagnetism, PF (b) FG vs PF, UWB

Fig.9 trajectory diagram

For the second stage, FG fusion positioning provides a lower mean positioning error than UWB positioning from Table.2 and Fig.7. In terms of mean positioning error, the mean positioning error of FG fusion positioning method is 1.52m and 1.66m, which is reduced by 7.3% and 5.0% in Ex 1# and Ex 2#; in terms of STD of positioning error, positioning points error of FG has a smaller STD, which indicates there is less hopping points; in terms of CDF of positioning error, reference points of UWB positioning error is within 2m account for 73% and 58%, which is lower than that of FG by 79% and 71%. From the trajectory of Ex 1# and Ex 2#, the positioning accuracy of UWB decreases seriously on the left side of the BS block area and there are some hopping points. However, the trajectory of FG is closer to the real trajectory. Part of hopping points are eliminated obviously. Therefore, FG fusion positioning algorithm mainly solves the problem of UWB positioning hopping points with large positioning error.

IV. Conclusion

In this paper, a two-stage fusion localization model for UWB/PDR/geomagnetism is proposed in the special environment of underground space. PDR/geomagnetism combination positioning is realized by using the improved PF algorithm based on regional constraints, and it is further fused with the UWB localization results by FG. The experimental results show that the proposed improved PF combination algorithm can effectively improve the positioning accuracy and algorithm efficiency. After FG fusion, the positioning hopping points with error over 2m are decreased and it effectively improves the problem of attenuation of positioning accuracy due to signal occlusion in some areas of UWB. Finally, the proposed two-stage fusion positioning model in this paper can be combined with other mainstream positioning technique according to the actual environment and the need for positioning.

V. Acknowledgments

This work is supported by the Elastic Architecture Design and Key Technology V erification of PNT System Project (2020YFB0505800).

VI. Reference

[1] Vallivaara I, Haverinen J, Kemppainen A, Roning J. Simultaneous Localization and Mapping Using Ambient Magnetic Field [C] //IEEE International Conference on Multisensor Fusion and Integration for Intelligent Systems, Salt Lake City, Utah, USA, 2010.

[2] O. Schneider, "Requirements for positioning and navigation in underground constructions," 2010 International Conference on Indoor Positioning and Indoor Navigation, Zurich, Switzerland, 2010, pp. 1-4, doi: 10.1109/IPIN.2010.5646747.

[3] Kunhoth J,Karkar A G,Al-maadeed S, et al. Indoor positioning and wayfinding systems:a survey[J].Human-centric Computing and Information Sciences, 2020,10(1):

doi:10.1186/s13673-020-00222-0.

[4] Ashrafi I , Hur S , Park Y. Smartphone sensor based indoor positioning: current status , opportunities , and future challenges[J]. electronics,2020,9(6): 891-919.

[5] Xi R , Li Y J , Hou M S. Survey on indoor localization[J]. computer Science.2016,43(4).

[6] Guo N, Jiang W, Li J, Liu F, Dong J. Research on the UWB High Precision Indoor Positioning Method with the Heterogeneous Information Constraints[J]. Journal of Global Positioning Systems. 2021, 17(2). DOI: 10.5081/jgps.17.2.164.

[7] Wang Y, Li X, Zou J, et al. A foot-mounted inertial measurement unit(IMU)positioning algorithm based on magnetic constraint[J]. Sensors,2018,18(3):741.

[8] Song B, Cheng Lei, Zhou M D et al. The design of cellphone indoor positioning system based magnetic assisted inertial navigation technology [J]. Journal of sensing technology, 2015,28(8) :1249-1254.

[9] Gao J X, Chang M Y. Geomagnetism and PDR localization algorithm based on smart phone [J]. Modern surveying and mapping, 2020,43(4).

[10] Wang Z Y, Gao J X, Li Z K et al. An indoor localization method combining WIFI, geomagnetism and PDR[J]. Surveying and mapping notification, 2020(6) :17-21.

[11] Yang Z. Study on high precision indoor positioning technology based on UWB/MEMS [D]. China University of Mining and Technology,2015.

[12] Zhu C J. Research on indoor poditioning technology of UWB/MEMS [D]. People's Liberation Army Information engineering University,2017(7).

[13] H. Benzerrouk and A. V. Nebylov, "Robust IMU/UWB integration for indoor pedestrian navigation," 2018 25th Saint Petersburg International Conference on Integrated Navigation Systems (ICINS), St. Petersburg, Russia, 2018, pp. 1-5, doi: 10.23919/ICINS.2018.8405844.

[14] D. Gao, A. Li and J. Fu, "Analysis of positioning performance of UWB system in metal NLOS environment," 2018 Chinese Automation Congress (CAC), Xi'an, China, 2018, pp. 600-604, doi: 10.1109/CAC.2018.8623602.

[15] Daquan Feng, Junjie Peng, Yuan Zhang et al. An Adaptive IMU/UWB Fusion Method for NLOS Indoor Positioning and Navigation[J]. IEEE Internet of Things Journal, 2023.

[16] M. Liao, Y. Li, G. Wang, Z. Lei and Z. Zhang, "An Indoor Positioning Algorithm Against NLOS Error Based on UWB," 2022 41st Chinese Control Conference (CCC), Hefei, China, 2022, pp. 5140-5145, doi: 10.23919/CCC55666.2022.9902618.

[17] Oliveirah H, Dias S S,Bruno M. Cooperative terrain navigation using hybrid gmm/smc message passing on factor graphs[J]. IEEE Transcations on Aerospace and Electronic Systems, 2020, 56(5):3958-3970.

[18] Fan S, Zhang Y, Yu C, et al. An advanced cooperative positioning algorithm based on improved factor graph and sum-product theory for multiple AUVs[J]. IEEE Access, 2019, 7: 67006-67017.

[19] Kschischang F R, Frey B J, Loeliger H A. Factor graphs and the sum-product algorithm[J]. IEEE Transactions on Information Theory, 2001, 47(2):498-519.

[20] Zhou Y J, Z Qing H, LIU J Y, SUN K C. Develop of factor and its application technology in positioning and navigation [J]. Global positioning system, 2020(2):45.

[21] TANNER R A. An introduction to factor graphs[J]. IEEE Signal Processing Magazine, 2004, 21(1):28-41. DOI:10.1109/MSP.2004.1267047.

[22] WIBERG N, LOELIGER H A, KOTTER R. Codes and iterative decoding on general graphs[J]. European Transcations on Telecommunications, 1995, 6(5):513-525. DOI:10.1002/ett. 4460060507.

[23] Ye, P, Zhan, X. Q, Zhang, Y. H. Mended EKF-based GPS/INS Tight Coupling Simulator[C], International Conference on Advanced Materials and Information Technology Processing, 2011, 271-273.

[24] Jiang, H. T, Shi, C, Li, T, Dong, Y. T, Li, Y. H, Jing, G. F. Low-cost GPS/INS integration with accurate measurement modeling using an

extended state observer[J]. Gps Solutions, 2021, 25.

Authors

JinkunLi was born in 1998, in China. He received the B.S. degree in Telecommunication Engineering from the Qingdao University of China, Qingdao, China, in 2020, and majored in Information and Telecommunication Engineering in Beihang University for master's degree, Beijing, China. His research direction is indoor positioning.

ChundiXiu was born in 1975, in China. She received the B.E. and M.E. degrees with the Department of Electrical Engineering, Harbin Institute of Technology in 1997 and 1999, respectively, and the Ph.D. degree in the School of Automation Science and Electrical Engineering, Beihang University, China, in 2003. From 2004 to 2005, she was a postdoctoral research fellow with the Department of Electronic Engineering, Tsinghua University. She has worked as a lecturer in the School of Electronic and Information Engineering, Beihang University since 2006. She was a visiting scholar at the University of Sydney from 2016 to 2017. Her research interests include wireless communications, satellite communications, wireless positioning and navigation.

DongkaiYang was born in 1972, in China. He received the B.S. degree in Electronic Engineering from the North University of China, Taiyuan, China, in 1994, and the M.S. and Ph.D degrees in Communication and Information Systems from Beihang University, Beijing, China, in 1997 and 2000, respectively. From 2001 to 2002, he was a Research Fellow with the Nanyang Technological University, Singapore. Since 2010, he has been a full-time professor at the School of Electronic and Information Engineering at Beihang University. His interests include the Global Navigation Satellite System (GNSS) and its applications.

Maria S. Selezneva received M.S. and Ph.D degrees in intelligent navigation systems from Bauman Moscow State Technical University, Moscow, Russia, in 2015 and 2018, respectively. She has been with the Department of Automatic Control Systems, Bauman Moscow State Technical University since 2018, as an Associate Professor. Her research interests include genetic algorithm and intelligent navigation of aircraft. Dr. Selezneva was the recipient of the Russian Government Prize in the field of science and technology for young scientists in 2019.

Journal of Global Positioning Systems (*2022*)
Vol. 18, No.2: 134-135

Ocean Wind Vector Retrieval Based on Spaceborne Global Navigation Satellite System Reflectometry

Guodong Zhang, Email: guodongzhang_q@163.com
Supervisor: **Dr. Dongkai Yang**
University: **Beihang University**
Defense Date: **May 26, 2022**

Abstract

Global Navigation Satellite System Reflectometry (GNSS-R) uses GNSS signals as the microwave remote sensing signal source to detect physical parameters of the global surface. GNSS-R is an organic fusion of navigation and remote sensing, an innovative application of GNSS signals. GNSS-R has the advantages of all-weather, multiple signal sources, high spatial and temporal resolution, which is beneficial to be carried on microsatellite platforms.

The ocean wind vector is an important part of ocean dynamic parameters. Accurate ocean wind vector detection plays a vital role in the early warning and forecasting of marine dynamic disasters. The research of ocean wind vector retrieval using spaceborne GNSS-R is helpful for the realization of global high temporal and spatial resolution ocean wind detection, which has important practical significance and urgent national needs. Although a lot of research and progress has been made in ocean wind vector retrieval using spaceborne GNSS-R, there are still many problems before commercial application, such as wind speed accuracy and wind direction retrieval, which hinder its popularization and application. Aiming at these problems, the main research contents and achievements of this thesis are as follows:

(1) In order to make spaceborne GNSS-R cyclone wind research get rid of the dependence on the prior information of whether the cyclone event occurs, a single-pass cyclone event detection algorithm using spaceborne GNSS-R full delay-Doppler map (DDM) is presented. The study focuses on investigating the influence of cyclone on the spaceborne GNSS-R full DDM. An observable is defined to describe full DDM asymmetry, and demonstrated to be sensitive to cyclone event using the simulator. The proposed method is based on a time sliding window to detect the full DDM asymmetry anomalies. The results show that cyclone event can be detected by the algorithm. These results provide information to guide the high wind speed retrieval in real-time using spaceborne GNSS-R.

(2) Spaceborne GNSS-R ocean wind speed retrieval has the problems of high data quality control standards and low accuracy of high wind speed. Based on the cyclone event detection algorithm, an

ocean wind speed retrieval algorithm based on ocean state is presented. The ocean state types are divided into conventional ocean state and cyclone ocean state. Before wind speed retrieval, the cyclone monitoring algorithm is used to identify the ocean state type. Then, the ocean wind speed is retrieved using the empirical geophysical model function of different ocean state types. The retrieval accuracy of high wind speed is improved while the retrieval accuracy of medium and low wind speed is ensured. The wind speed retrieval algorithm is suitable for spaceborne real-time retrieval.

(3) There are few studies on the ocean wind direction retrieval using spaceborne GNSS-R, because the specular reflection signal is not sensitive to the sea surface wind direction. The wind direction retrieval algorithms using spaceborne GNSS-R in non-specular geometry are presented. The sensitivity of the scattered GNSS signal in the non-specular geometry to wind direction is analyzed. The sub-satellite non-specular observation mode is constructed. The observable that is sensitive to wind direction in this mode is defined. A wind direction retrieval algorithm based on wind speed and a wind vector retrieval algorithm based on maximum likelihood estimation are constructed. It solves the problem that the specular reflection signal is difficult to retrieve the wind direction and can achieve real-time wind direction retrieval using spaceborne GNSS-R.

(4) In order to meet the needs of real-time processing and fast retrieval of ocean wind vector using spaceborne GNSS-R, the spaceborne GNSS-R fast retrieval software for ocean wind vector is designed and implemented. The data processing system including cyclone event detection, ocean wind speed retrieval and ocean wind direction retrieval is constructed. It can provide a reliable and stable application software for the research and application of ocean wind vector real-time retrieval using spaceborne GNSS-R.

Keywords: GNSS-R, Cyclone event, Ocean wind speed, Ocean wind direction, Remote sensing

Journal of Global Positioning Systems (*2022*)
Vol. 18, No.2: 136-137

Journal of Global Positioning Systems
2022
© CPGPS

Enhancing the Accuracy of Water Vapour Retrieval from Remote Sensing Observations Using Ground-based GNSS Data

Jia He
Supervisor: **Dr. Zhizhao Liu**
Graduate Date: **December 2021**
University: **Department of Land Surveying and Geo-Informatics**
Hong Kong Polytechnic University
Web-page: **https://theses.lib.polyu.edu.hk/handle/200/11218**

ABSTRACT

Water vapour, as the fundamental element and one of the most important natural greenhouse gases in the atmosphere, is vital for heat and moisture fluxes. Improved knowledge of water vapour and its variability on the different temporal-spatial scales is essential for climate and environmental research. Water vapour content can be estimated through radiosonde balloons, microwave-radiometers, sun-photometers, Global Navigation Satellite Systems (GNSS) / Global Positioning Systems (GPS), and remote sensing satellites. These observation instruments provide products with different but complementary characteristics. For instance, radiosonde and GNSS/GPS observations are usually considered as ground truth because of their high precision, but their applications are restricted by the locations of the stations. Remote sensing observation, on the other hand, is the most efficient means of water vapour observation on the global scale but with a larger retrieval error. The core research aim is to enhance the water vapour retrieval accuracy from remote sensors. Special weight was put on water vapour observation from Near Infrared (NIR) channels.

A novel retrieval method has been developed for the Moderate Resolution Imaging Spectro-radiometer (MODIS) onboard the Terra and Aqua satellite platforms in this research based on empirical regression analysis. This new approach provides an effective way to retrieve water vapour without pre-obtained atmospheric information. Water vapour data observed during 2003 ~ 2017 from 464 GPS stations located in western North America and their spatial-temporal collocated MODIS level 1 reflectance data were employed as training data for model development. The training data were resampled into 10 subsets using the bootstrap method. The regression functions trained by these independent subsets reduced the uncertainty in the model training and minimized the sensitivity of possible channel drifting. Verifications in North America show that the root mean square error (RMSE) for water vapour calculated from MODIS/Terra reduces 48.12% to 2.362 mm when using two-channel ratio transmittance and 50.74% to 2.243 mm when using three-channel ratio transmittance. The RMSE for water vapour calculated from MODIS/Aqua reduces 42.54% to 2.562 mm and 42.99% to 2.541 mm when using two-channel and three-channel ratio transmittance, respectively. Validations over five additional stations also show that the overall RMSE for MODIS/Terra data reduces 22.80% to 5.946 mm when using two-channel ratio transmittance, and 21.69% to 6.006 mm when using three-channel ratio

transmittance. For MODIS/Aqua data, the reductions are 16.42% to 6.010 mm when using two-channel ratio transmittance and 15.26% to 6.094 mm when using three-channel ratio transmittance.

The retrieval algorithm was also validated in Australia and its neighbouring area for the first time. The observation results over 2017 ~ 2019 have clearly shown that our new ensemble-based empirical regression model, which was developed using data from the North Hemisphere, is still valid in the South Hemisphere. For the data obtained from MODIS/Terra, the RMSE has reduced by 58.53% from 5.712 mm to 2.369 mm when using 2-channel ratio transmittance and has reduced by 56.14% to 2.505 mm using 3-channel ratio transmittance, respectively. For the data obtained from MODIS/Aqua, the RMSE has reduced by 49.17% from 5.170 mm to 2.628 mm using 2-channel ratio transmittance and has reduced by 46.60% to 2.761 mm using 3-channel ratio transmittance, respectively. The results further prove that the newly proposed retrieval model has very good property of having no temporal or spatial dependency over a large observation area. The coefficients can be easily applied to areas of interest without pre-calculated input parameters of atmospheric profiles. It is reasonable to conclude that this algorithm provides an effective way to retrieve water vapour globally under cloud-free condition.

On the other hand, as the surface spectral reflectance is one of the error sources for water vapour retrieval, regression functions trained for different land cover types adapted from MCD12Q1 IGBP legend are discussed. Thus, the bias for MODIS NIR channels could be further reduced. Validations in North America show that for data calculated from MODIS/Terra, the RMSE reduced 50.78% to 2.229 mm for data using two-channel ratio transmittance and 53.06% to 2.126 mm for data using three-channel ratio transmittance. For data obtained from MODIS/Aqua, the RMSE reduced 45.54% to 2.423 mm when using two-channel ratio transmittance and 45.34% to 2.432 mm when using three-channel ratio transmittance.

Last but not least, the empirical regression method was implemented for water vapour observation from MERSI/FY-3B NIR channels. The collocated MERSI L1b reflectance data in the NIR channels are used for water vapour retrieval. PWV data observed from 256 ground-based GPS stations located in the western North America in 2016 are used as reference data for model development. Then, validation is performed with data obtained during 2017 ~ 2019 from both the western North America and Australia to assess the performance of the proposed algorithm. The results indicate that the new PWV results agree very well with ground based PWV reference data. The mean absolute percentage error (MAPE) for ensemble median PWV is 16.72% ~ 36.74% in western North America and is 15.47% ~ 32.31% in Australia. The RMSE is 4.635 mm ~ 8.156 mm in western North America and is 5.383 mm ~ 8.900 mm in Australia. The weighted mean value using three-channel ratio transmittance has the best retrieval accuracy, with RMSE of 4.635 mm in western North America and 5.383 mm in Australia. Together with MERSI onboard of other FY series, more information on water vapour distribution on the global scale would be provided for climate and environmental research.

Journal of Global Positioning Systems (2022)
Vol. 18, No.2:138-139

GNSS PPP/INS Integrated Precise Positioning and Attitude Determination with Comprehensive Error Analysis

Lingxuan Wang, Email: wlx@whu.edu.cn

Supervisors: Prof. **Erhu Wei**, Prof. **Jianguo Wang (York University)**, Prof. **Jingnan Liu**

University: **School of Geodesy and Geomatics, Wuhan University**

Defense Date: **December 2022**

Abstract

GNSS Precise Point Positioning (PPP) has attracted widespread attention for its advantages of low cost and high precision at wide-area. However, the solution of PPP ambiguity parameters requires a long convergence time. Due to the inherent vulnerability of GNSS, frequent re-initialization under dynamic conditions seriously affects its positioning and navigation performance. To meet the current requirements, a multi-sensor integrated approach with high precision, high reliability, and high integrity has become a necessary trend for the development of the industry. Inertial Navigation System (INS) has the advantage of high precision in the short term, so it is complementary to GNSS and provides a solution to overcome the shortcomings of PPP in dynamic situations. As an essential scope of the multi-sensors integrated navigation systems research, PPP/INS has been studied and applied extensively. However, several core problems still need to be solved, mainly reflected in the high-reliability algorithms, weight determination of different systems, comprehensive error analysis methods, quality control and accuracy evaluation methods for the filtering process, and so on. Such problems are bottlenecks restricting the development and application of high-precision PPP/INS integrated systems, which have been the research hotspots and challenging topics in recent years. This thesis researches the problems mentioned above, and the main contents and contributions can be summarized as follows.

(1) Cycle slip detection is the premise to ensure the high precision positioning performance of PPP. Thus, a detailed error analysis is carried out for the INS-aided cycle-slip detection term. The specific influence of INS error on the cycle-slip detection term and detection performance are revealed, and the INS-aided cycle-slip detection terms suitable for PPP dynamic navigation application are constructed. Furthermore, a targeted detection threshold is derived. Experimental results show that the proposed algorithm can enhance the performance of PPP cycle-slip detection and reduce the risk of false alarms and missing detection.

(2) A PPP ambiguity resolution enhancement algorithm is proposed based on the virtual observation equation with INS position constrained. When GNSS signals are recaptured, the ambiguity parameters need to be reset. And the error accumulation of INS during the GNSS lock-out period will significantly affect the refixation of ambiguity parameters. From the error propagation analysis of INS independent navigation, a stochastic model for the virtual observation equation with INS position-constrained is constructed according to the time

of loss of lock. The stochastic model can more accurately reflect the characteristics of INS errors so that INS can always play a positive role in PPP ambiguity resolution process. Even if the INS error reaches several meters, it will not degrade the performance of the PPP itself. Based on this research, the enhanced ambiguity resolution strategy for the integrated system is discussed. And the PPP/INS integrated ambiguity resolution enhancement algorithm is subsequently proposed. Several measured vehicle navigation data have been used to evaluate the algorithm.

(3) The traditional Kalman filtering method only relies on the innovation vector for quality control and cannot fully consider the filter modeling error. A novel Kalman filtering process is used to achieve the unified posterior estimation of process noise, observation noise, and innovation vector. And the redundant observation factor of each noise can be accurately calculated by this process. A variance component estimation (VCE) method for the Kalman filter is proposed based on this, which comprehensively considers the redundant observation factors of various noise items and solves the problem of oversimplification of the previous VCE methods. The proposed method can directly estimate the variance components of the multi-source observations in the filter and realize the weight determination of the multi-source information. Taking multi-frequency and multi-system GNSS PPP static positioning as an example, the experimental analysis is carried out. The results show that the variance-covariance matrix of various observation and state-predicted values can be reasonably adjusted according to the calculated process noise residuals, observation residuals, and innovation vectors. And the positioning accuracy is improved significantly.

(4) A novel GNSS PPP/INS integration strategy is proposed employing the rigid body nonlinear kinematic equation. In the current GNSS/INS integrated filtering model, the observations of the two different systems are processed in the time update and measurement update processes, respectively. And the INS observation with errors directly constitutes the state transition matrix, which brings systematic errors but cannot be effectively eliminated. At the same time, the two systems cannot achieve the posterior estimation of the variance-covariance components. It is the only way to balance the contributions of different systems by tedious adjusting them through prior information and experience values. This thesis constructs a novel PPP/INS integrated state model and observation equation using the direct Kalman filtering method considering the kinematic relationship between state parameters. The new approach is more in line with the Kalman filtering theory. It has a more straightforward structure, which is convenient for providing dynamic model constraints for INS. It also can significantly reduce the impact of random drift of INS on the integrated system. At the same time, it is convenient to obtain a comprehensive error analysis of each noise in the filtering process and solve the weight determination problem for the different types of observation in the integrated system.

Keywords: GNSS PPP; INS; Integrated precise positioning and attitude determination; Kalman filter; Comprehensive error analysis; Novel integration strategy

Journal of Global Positioning Systems (2022)

Vol. 18, No.2: 140:142

An Investigation of Real-time GNSS Precipitable Water Vapor Retrievals

Peng Sun, Email: peng_sun@cumt.edu.cn

Supervisor: **Dr. Kefei Zhang**

University: **School of Environment Science and Spatial Informatics**

China University of Mining and Technology

Defense Date:

Abstract

Water vapor, the content of which can be measured by precipitable water vapor (PWV), is a greenhouse gas in the troposphere, a carrier of atmospheric energy exchange, and a material basis of weather changes. When the signals of Global Navigation Satellite Systems (GNSS) propagate through the troposphere, the tropospheric delay, as a major error source of GNSS positioning, occurs resulting from both the dry component and water vapor in the troposphere. As a result, the water vapor information is embedded in the GNSS signals, and all-weather high-accuracy tropospheric delay and PWV products can be obtained from GNSS data processing for weather and climate change research, which is low-cost compared to other water vapor monitoring techniques.

For the purpose of time-critical extreme weather prediction, GNSS real-time precise point positioning (PPP) has become a powerful technique for the determination of the zenith tropospheric delay (ZTD) over a GNSS station of interest, and the subsequent high-accuracy retrieval of PWV. This paper mainly focuses on the high-accuracy atmospheric modeling, development of real-time PPP software and the assessment of accuracy of the resulted ZTD, refinement of ZHD interpolation method for obtaining high-accuracy ZHD (zenith hydrostatic delay) from VMF1/VMF3 forecasting grids, ZWD (zenith wet delay)-PWV conversion model and the accuracy of PWV resulting from the VMF1/VMF3-based ZHD and the conversion model, and the relation between the real-time GNSS-PWV and weather changes. The details are as follows:

(1) In most of the empirical models, atmospheric pressure at the user site is typically obtained from atmospheric pressure at a reference height combined with an atmospheric pressure vertical reduction model. If the reference height largely differs from the height of the user site, the quality of the predicted atmospheric pressure is usually poor due to the simple reduction model used. In this study, a voxel-based atmospheric pressure model, named PVoxel, was developed for obtaining better accuracy atmospheric pressures using sample data of 10-year ERA5 monthly mean data, totaling 120 monthly mean values in the temporal domain. Each monthly mean atmospheric pressure and virtual temperature at each of the four selected reference heights over all globally distributed grid points (horizontal resolution: 1°×1°), i.e., at the nodes of the 3D voxels, were determined. Then the characteristics of the annual and semi-annual variation in both atmospheric pressure and virtual temperature in the temporal domain for each node were modeled. The PVoxel model developed is 4-dimensional, thus it can be used to predict atmospheric pressure at a given geographic position and any altitude, and any time. The model was evaluated by comparing the atmospheric pressures predicted for the sites of all globally distributed radiosonde stations against their corresponding radiosonde data of the sites. The model predicted results were also compared with that of the

widely used models like GPT3, UNB3m et al. and the comparison results showed that PVoxel outperformed these models, especially at high altitudes. The significant performance improvement of the new model is promising for an improvement in its resultant ZHD, which is significant for obtaining more accurate position (especially the height component) and zenith tropospheric delay.

(2) A modified BNC software (BNC_MET) was developed for real-time retrieval of GNSS-PWV. Compared to the original open-source BNC software, the error correction, quality control and parameter estimation modules were significantly improved in the new development. Two experiments were designed for the evaluation of real-time ZTD estimated by the modified BNC software. Firstly, the accuracy of ZTD resulting from four different real-time service (RTS) products were evaluated using GPS-only and GPS+GLONASS real-time PPP. Compared to the IGS final tropospheric products, the mean RMSE of ZTD resulting from GPS-only and GPS+GLONASS PPP using CNES RTS products were 8.4 mm and 8.1 mm, respectively, while the corresponding RMSEs were 7.4 mm and 7.0 mm compared to the CODE tropospheric products. High accuracy ZTD (but slightly worse than the CNES ones) were also obtained from PPP using GFZ and WHU products, and the IGS03 performed the worst. Secondly, the accuracy of ZTD estimated by BDS-only PPP and GPS+BDS PPP were also evaluated using GFZ RTS products. The results showed that the accuracy of BDS-only PPP-resulted ZTD was slightly worse than that of GPS-only ones, and the GPS+BDS scheme performed better than GPS-only and BDS-only schemes.

(3) Refinement of ZHD interpolation method for VMF1/VMF3 forecasting grids. VMF1 and VMF3 forecasting grids provide ZHD, ZWD and mapping function coefficients at globally distributed grid points. However, a unified atmospheric pressure vertical correction coefficient was adopted by the official code provided by the data-provider. As a result, large ZHD prediction errors were obtained in some places. The ZHD vertical correction part during the interpolation was improved by two new methods. Firstly, atmospheric pressure vertical correction coefficient at each of the grid point were fitted and modeled for the vertical correction of VMF-based ZHD. Secondly, 3D-voxel based atmospheric temperature model from the above-mentioned PVoxel model were used for the ZHD vertical correction. The newly proposed methods were evaluated by surface atmospheric pressure observations from 2019 to 2021 at 404 radiosonde stations. For the first method, the mean RMSE of ZHD interpolated from VMF1, VMF3(5°×5°) and VMF3(1°×1°) forecasting grids were reduced from 5.5 mm, 4.9 mm and 3.9 mm to 3.7 mm, 4.2 mm and 3.6mm, respectively, while the maximum RMSE were reduced from 4.01 cm, 4.24 cm and 1.95 cm to 1.63 cm, 2.38 cm and 1.83 cm, accordingly. For the second method, the mean RMSEs were reduced to 3.6, 4.3 and 3.7 mm, respectively, and maximum ones were reduced to 1.64, 2.38 and 1.83 cm, respectively. Both the two newly proposed methods outperformed the traditional method. In addition, three horizontal interpolation methods were also evaluated, and the bilinear interpolation performed the best.

(4) A new weighted mean temperature (T_m) model, named GGNTm, considering the nonlinear variation of T_m in the vertical direction was established using 10-year long ERA5 monthly-mean reanalysis data. A three-order polynomial function was utilized to fit the vertical nonlinear variation in T_m at the grid points, and the temporal variation in each of the four coefficients in the T_m fitting function was also modeled with the variables of the mean, annual, and semi-annual amplitudes of the 10-year time series coefficients. The performance of the new model was evaluated using its predicted T_m values in 2018 to compare with the following two references in the same year: (1) Tm from ERA5 hourly reanalysis with the horizontal resolution of 5°×5°; (2) T_m from atmospheric profiles from 428 globally distributed radiosonde stations. Compared to the first reference, the mean RMSEs of the model-predicted T_m values over all global grid points at the 950 and 500 hPa pressure levels were 3.35 and 3.94 K, respectively. Compared to the second reference, the mean bias and

mean RMSE of the model-predicted T_m values over the 428 radiosonde stations at the surface level were 0.34 and 3.89 K, respectively; the mean bias and mean RMSE of the model's T_m values over all pressure levels in the height range from the surface to 10 km altitude were 0.16 and 4.20 K, respectively. Results indicated that significant improvements made by the new model were at high-altitude pressure levels.

(5) The accuracy of the GNSS-retrieved real-time PWV using ZHD from VMF forecasting grid and T_m from GGNTm was also investigated. GPS observations from 41 IGS stations that have co-located radiosonde stations during the period of the first half of 2020 were used to test the quality of GPS-PWV. The results showed that mean RMSE of the PWVs resulting from GPS-PPP was smaller than 2mm compared to reference PWVs from collocated radiosonde data, which is accurate enough for meteorological applications.

(6) The correlation between real-time GNSS-PWV and weather change was analyzed using 20-day-long real-time PWV obtained from 11 CORS stations in Hong Kong. The atmospheric pressures measured by co-located meteorological sensors were used for the calculation of ZHD and GGNTm model was used for the conversion of ZWD to PWV. By comparing the real-time PWV to the weather records provided by Hong Kong Observatory, it can be concluded that the real-time PWVs are tightly correlated to weather change.

The accuracy of real-time PWV can be improved by implementing the above-mentioned research, which may make significant contributions to weather forecasting and the time-critical severe weather monitoring.

This dissertation includes 56 figures, 23 tables and 203 references.

Keywords: zenith tropospheric delay; precise point positioning; zenith hydrostatic delay; weighted mean temperature; precipitable water vapor

Volume 18, No. 2, 2022

Journal of Global Positioning Systems

Published by

International Association of Chinese Professionals in Global Positioning Systems (CPGPS)

ISSN 1446-3156 (Print version)

ISSN 1446-3164 (CD-ROM Version)